Cell

Conservation of Ca^{2+}/Calmodulin Regulation across Na and Ca^{2+} Channels

Manu Ben-Johny,[1] Philemon S. Yang,[1] Jacqueline Niu,[1] Wanjun Yang,[1] Rosy Joshi-Mukherjee,[1] and David T. Yue[1,*]
[1]Calcium Signals Laboratory, Departments of Biomedical Engineering and Neuroscience and Center for Cell Dynamics,
The Johns Hopkins University School of Medicine, Ross Building, Room 713, 720 Rutland Avenue, Baltimore, MD 21205, USA
*Correspondence: dyue@jhmi.edu
http://dx.doi.org/10.1016/j.cell.2014.04.035

SUMMARY

Voltage-gated Na and Ca^{2+} channels comprise distinct ion channel superfamilies, yet the carboxy tails of these channels exhibit high homology, hinting at a long-shared and purposeful module. For different Ca^{2+} channels, carboxyl-tail interactions with calmodulin do elaborate robust and similar forms of Ca^{2+} regulation. However, Na channels have only shown subtler Ca^{2+} modulation that differs among reports, challenging attempts at unified understanding. Here, by rapid Ca^{2+} photorelease onto Na channels, we reset this view of Na channel regulation. For cardiac-muscle channels ($Na_V1.5$), reported effects from which most mechanistic proposals derive, we observe no Ca^{2+} modulation. Conversely, for skeletal-muscle channels ($Na_V1.4$), we uncover fast Ca^{2+} regulation eerily similar to that of Ca^{2+} channels. Channelopathic myotonia mutations halve $Na_V1.4$ Ca^{2+} regulation, and transplanting the $Na_V1.4$ carboxy tail onto Ca^{2+} channels recapitulates Ca^{2+} regulation. Thus, we argue for the persistence and physiological relevance of an ancient Ca^{2+} regulatory module across Na and Ca^{2+} channels.

INTRODUCTION

Voltage-gated Na and Ca^{2+} channels constitute two prominent ion channel superfamilies (Jan and Jan, 1989), each subserving distinct functions (Adams and Snutch, 2007; Hille, 2001; Jan and Jan, 1989). Curiously, however, the carboxy tails of these channels (Figure 1A, CI region) demonstrate high sequence homology, hinting at a tangible ancestral blueprint. Babitch first remarked on a conserved vestigial EF hand (Babitch, 1990) (rose shading), and further scrutiny reveals extensive homology throughout. The CI region contains dual vestigial EF hand motifs (Babitch, 1990; Chagot et al., 2009; de Leon et al., 1995; Miloushev et al., 2009) (rose, green) and a calmodulin (CaM)-binding IQ domain (Mori et al., 2000; Zühlke and Reuter, 1998) (lavender). If this homology were to support functions of like correspondence, deep mechanistic insights could be gleaned from combined investigation of Na and Ca^{2+} channels and shared principles obtained for approaching related channelopathic diseases.

Ca^{2+} channels have largely fulfilled this possibility, as the CI regions of channels across this superfamily elaborate rapid and robust Ca^{2+}-dependent regulation (Dunlap, 2007), often manifest as Ca^{2+} current inactivation (Eckert and Chad, 1984) (Ca^{2+}-dependent inactivation, CDI). A single Ca^{2+}-free CaM (apoCaM) preassociates with the IQ and other CI elements in the channel carboxy terminus (Erickson et al., 2001; Mori et al., 2004; Pitt et al., 2001). This arrangement renders CaM as a resident Ca^{2+} sensor poised for modulation. Subsequent Ca^{2+} binding to this CaM triggers CI rearrangements that inhibit channel opening (Ben Johny et al., 2013). Intriguingly, regulation can be induced by Ca^{2+} binding to one lobe of CaM or the other (DeMaria et al., 2001; Peterson et al., 1999; Yang et al., 2006), substantiating a functional bipartition of CaM discovered in *Paramecium* (Preston et al., 1991). For illustration, Figures 1B and 1C display the CDI of $Ca_V1.3$ channels. Ca^{2+} channels themselves convey the Ca^{2+} that induces CDI (Figure 1B), and fluxing Ba^{2+} serves as negative control (Ba^{2+} binds CaM poorly [Chao et al., 1984]). Accordingly, Ca^{2+} currents decline sharply via CDI (Figure 1C, left, red trace), but not Ba^{2+} currents (black trace). The steady-state extent of CDI (r_{300}) thereby exhibits a hallmark U-shaped voltage dependence (Figure 1C, right, red) (Eckert and Chad, 1984). Such regulation influences excitability of heart (Alseikhan et al., 2002), rhythmicity and neurotransmission in brain (Borst and Sakmann, 1998; Huang et al., 2012), and many other processes (Adams and Snutch, 2007; Crotti et al., 2013).

By contrast, for Na channels (Deschênes et al., 2002; Tan et al., 2002), the existence, functional nature, and postulated mechanisms of Ca^{2+} modulation have eluded consensus. Some find that muscle Na channels are not Ca^{2+} regulated (Herzog et al., 2003); others describe subtle Ca^{2+} modulation of inactivation (Van Petegem et al., 2012). Where Ca^{2+} effects have been observed, the proposed identity of the Ca^{2+} sensor for regulation varies. Unlike Ca^{2+} channels, some propose that Ca^{2+} binding to the first vestigial EF hand in Na channels induces Ca^{2+} regulation (Biswas et al., 2009; Tan et al., 2002; Wingo et al., 2004), but this view has not been universally accepted (Kim et al., 2004b; Miloushev et al., 2009). Instead, others emphasize Ca^{2+} binding to CaM as the trigger (Kim et al., 2004a; Sarhan et al., 2012; Shah et al., 2006), which is consistent with CaM binding to peptide fragments of channels (Feldkamp et al., 2011; Mori et al., 2000; Wang et al., 2012). Also contrasting with Ca^{2+} channels, a key structural determinant of Na channel regulation has

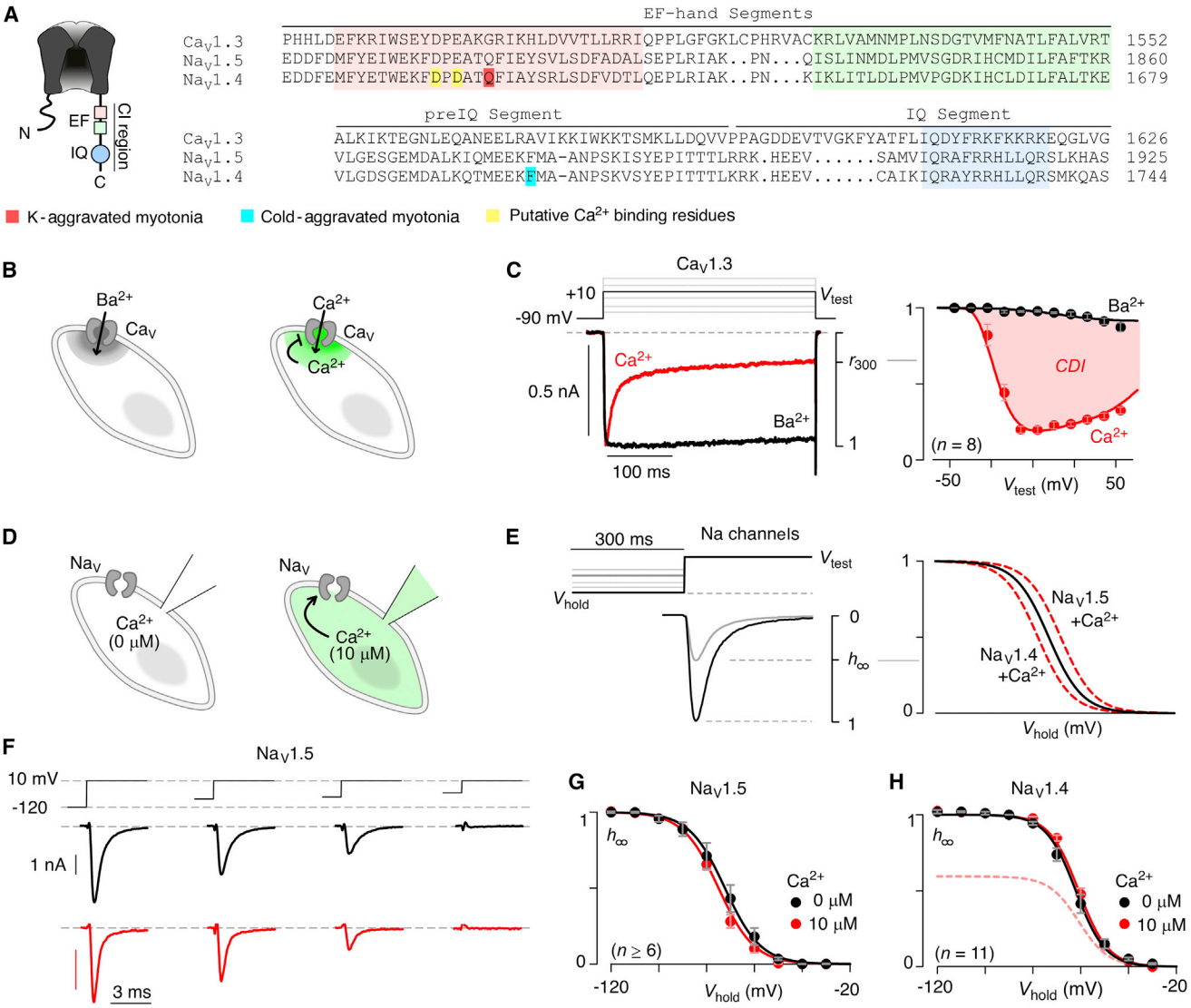

Figure 1. Homology but Divergent Function for Ca^{2+} versus Na Channels

(A) CI region of Ca^{2+} ($Ca_V1.3$) and Na channels ($Na_V1.5$ and $Na_V1.4$). Dual vestigial EF hands shaded in rose and green. IQ domain, blue.

(B) Ca^{2+} channel regulation inducible by channel Ca^{2+} influx. Ba^{2+} influx as negative control.

(C) Left, $Ca_V1.3$ current traces carried by Ca^{2+} (red) or Ba^{2+} (black). Vertical bar for Ca^{2+} trace. Ba^{2+} trace scaled ~3× downward for kinetic comparison. Right, r_{300} (fraction of peak current remaining after 300 ms depolarization) versus V_{test} potential, plotted as mean ± SEM (eight cells).

(D) Na channels characterized under pipet dialysis with 0 or 10 μM Ca^{2+}.

(E) Schematic of reported Ca^{2+} effects on inactivation. Left, h_∞, fractional current remaining after prepulses (V_{hold}). Right, purported Ca^{2+}-induced voltage shifts of h_∞.

(F) $Na_V1.5$ currents under protocol in (E) (black, 0 Ca^{2+}; red, 10 μM Ca^{2+} buffered with HEDTA). See Figure S1.

(G and H) Normalized form of h_∞ unaffected by Ca^{2+}. Potential Ca^{2+}-induced reduction in $Na_V1.4$ h_∞ (rose dashed line). Error bars, SEM throughout. Fit function: $h_\infty = 1/(1 + \exp((V_{hold} - V_{1/2})/SF)$, where SF = 6.2 ($Na_V1.4$) and 7.5 ($Na_V1.5$).

been suggested to reside outside the carboxy tail, in the III-IV loop (Sarhan et al., 2012). Others, however, emphasize a dominant role for the carboxy terminus (Biswas et al., 2009; Shah et al., 2006; Tan et al., 2002; Wingo et al., 2004). Lastly, when observed, Ca^{2+} regulation of Na channels has only been demonstrated in heterologously expressed recombinant channels, and no modulation has been directly demonstrated in native cells (Deschênes et al., 2002; Feldkamp et al., 2011; Mori et al., 2000; Sarhan et al., 2012; Wang et al., 2012). Compared to Ca^{2+} channels, this generally inconsistent Na channel landscape (Biswas et al., 2008, 2009; Potet et al., 2009; Sarhan et al., 2012; Tan et al., 2002; Van Petegem et al., 2012; Wingo et al., 2004) suggests divergence, weakening, or even loss of CI regulatory function (Van Petegem et al., 2012).

Here, we introduce two rapid Ca^{2+} delivery approaches to the Na channel field—Ca^{2+} photouncaging or Ca^{2+} influx through

neighboring Ca^{2+} channels. Results obtained through these methodologies suggest significant revisions to the current view of Ca^{2+} regulation of Na channels. In particular, the bulk of current mechanistic inferences has been drawn from extensive studies of cardiac Na channels ($Na_V1.5$). Yet, under the rapid Ca^{2+} delivery paradigms used here, we fail to detect Ca^{2+} modulation of either heterologously expressed recombinant $Na_V1.5$ channels, or corresponding native Na currents in cardiac myocytes. By contrast, for prevalent skeletal-muscle Na channels ($Na_V1.4$), also reputed to host rather subtle Ca^{2+} effects, we now observe fast and robust Ca^{2+} regulation that strongly resembles the regulation of Ca^{2+} channels. Indeed, transplanting the $Na_V1.4$ carboxy tail onto Ca^{2+} channels recapitulates Ca^{2+} regulation, further establishing this domain as a conserved modular element across channel superfamilies. Biologically speaking, channelopathic mutations for cold- and potassium-aggravated myotonias suppress $Na_V1.4$ Ca^{2+} regulation by 2-fold, and rapid Ca^{2+} delivery methods resolve Ca^{2+} regulation of native Na currents within skeletal myotubes. Thus, the carboxy tail of Na channels presents as a potential molecular therapeutic target for these myotonias and related disease. Altogether, this study highlights the commonality of CaM-dependent Ca^{2+} regulation between Na and Ca^{2+} channel superfamilies.

RESULTS

Na Channels Lack Apparent Ca^{2+} Regulation

We initially used current experimental approaches to re-examine Ca^{2+} regulation of the best-studied Na channels—$Na_V1.5$ that prevails in heart and $Na_V1.4$ from skeletal muscle. As a prelude, we carefully considered the chief experimental result from which most conclusions have been drawn—that Ca^{2+} regulation of these channels induces modest shifts in the steady-state properties of a traditional rapid inactivation process (Biswas et al., 2008; Deschênes et al., 2002; Potet et al., 2009; Sarhan et al., 2012; Van Petegem et al., 2012; Wingo et al., 2004). The core paradigm has been to measure the fraction of current (h_∞) remaining at a fixed test voltage (V_{test}), following long depolarization to a family of prepulse voltages (V_{hold}; Figure 1E, left subpanel). Plotting h_∞ versus V_{hold} then yields the steady-state inactivation relation (h_∞ curve) as schematically diagrammed by the black curve in Figure 1E (right subpanel). Because Na channels do not flux Ca^{2+}, testing for Ca^{2+} regulation requires comparison of normalized h_∞ curves measured in cells statically dialyzed with a pipet solution containing ~0 μM free Ca^{2+} concentration ($[Ca^{2+}]$), with those measured in other cells set to ~10 μM (Figure 1D). Ca^{2+} elevation reportedly shifts h_∞ curves by up to ~10 mV, rightward in the case of $Na_V1.5$ (Biswas et al., 2009; Potet et al., 2009; Sarhan et al., 2012; Shah et al., 2006; Wingo et al., 2004), and leftward for $Na_V1.4$ (Biswas et al., 2008; Deschênes et al., 2002). These Ca^{2+} effects are cartooned by the red dashed curves in Figure 1E (right subpanel).

Thus apprised, we noted that prior studies used EGTA or BAPTA as Ca^{2+} buffers to nominally set intracellular $[Ca^{2+}]$ between 1 and 10 μM (Biswas et al., 2009; Potet et al., 2009; Sarhan et al., 2012; Shah et al., 2006; Tan et al., 2002; Wingo et al., 2004), a range far above their dissociation constants (K_d = 67 nM for EGTA, and K_d = 192 nM for BAPTA [Bers et al., 2010]). This regime could be problematic for controlling Ca^{2+} (Figure S1A available online). We therefore revisited these experiments using the more appropriate Ca^{2+} buffer HEDTA (K_d = 4 μM [Bers et al., 2010]), thus ensuring $[Ca^{2+}]$ ~10 μM. Figures 1F and 1G show exemplar Na currents and population data specifying actual h_∞ curves for $Na_V1.5$ channels, expressed heterologously in HEK293 cells. Surprisingly, no difference is present in the curve measured with $[Ca^{2+}]$ ~0 μM ($V_{1/2}$ = −72.3 ± 3 mV) versus that with $[Ca^{2+}]$ ~10 μM ($V_{1/2}$ = −75.5 ± 1.2 mV). Figure 1H also demonstrates no Ca^{2+} effects for $Na_V1.4$ channels ($V_{1/2}$ = −62 ± 1.8 mV at $[Ca^{2+}]$ ~0 μM; $V_{1/2}$ = −60.8 ± 0.8 mV at $[Ca^{2+}]$ ~10 μM; Figure S1B).

This unexpected lack of Ca^{2+} regulation intensified the seeming deviation of function in Na versus Ca^{2+} channels. Still, closer inspection revealed that Ca^{2+} elevation in $Na_V1.4$ channels appeared to diminish test-pulse current density corresponding to the plateau of h_∞ curves at −120 mV, from −318 ± 98 pA/pF (n = 11) to −189 ± 33 pA/pF (n = 11). Thus, Ca^{2+} might scale down an unnormalized h_∞ curve (Figure 1H, red dashed curve). No such trend was found for $Na_V1.5$ (−474 ± 98 pA/pF at $[Ca^{2+}]$ ~0 [n = 6] versus −424 ± 60 pA/pF at $[Ca^{2+}]$ ~10 μM [n = 11]).

Rapid Uncaging of Ca^{2+} Unveils Ca^{2+} Effects on Na Channels

A core limitation of delivering Ca^{2+} via pipet dialysis regards the uncertainty of detecting Ca^{2+}-induced changes in current amplitude without corresponding voltage-dependent shifts. Current size may differ in one group of cells versus another for many reasons unrelated to Ca^{2+}. To obviate this limitation, we utilized rapid photouncaging of Ca^{2+} to produce step-like increases in intracellular $[Ca^{2+}]$, whose magnitude was simultaneously measured via Ca^{2+} fluorescent indicators (Tadross et al., 2013). Figure 2A displays the outcome for $Na_V1.5$ channels. Na currents (I_{Na}) were evoked every 100 ms by the voltage-pulse train above. Without Ca^{2+} uncaging, peak currents remained steady (gray dots), confirming stability of the preparation. UV uncaging of a large Ca^{2+} step to ~10 μM (vertical cyan line) failed to perturb subsequent Na currents comprising the black I_{Na} trace. On average, plots of steady-state current inhibition (*CDI*) versus Ca^{2+} step amplitude (bottom subpanel) corroborate the lack of Ca^{2+} regulation of $Na_V1.5$ in our experiments. Detailed kinetic analysis of Na currents within each pulse also showed no change on Ca^{2+} elevation (Figure S2A).

On the other hand, $Na_V1.4$ channels demonstrated a different outcome (Figure 2B). As baseline, peak currents remained steady without Ca^{2+} uncaging (gray dots). Here, however, Ca^{2+} uncaging to ~2 μM rapidly inhibited peak currents during the pulse train (black I_{Na} trace), with an inhibitory time course of ~100 ms (rose curve). Data averaged from many cells indicated a robust maximal *CDI* reaching ~0.35, with a half-maximal effect achieved at $K_{1/2}$ ~1.5 μM. The overall *CDI* –$[Ca^{2+}]$ relation defines a Hill function with steepness coefficient ~1.8 (black curve, bottom subpanel). This inhibition of Na current upon Ca^{2+} uncaging unveils a CDI whose time course resembles that of Ca^{2+} channels (compare rose curve in Figure 2B with Figure 1C). As expected of a mainly Ca^{2+}-dependent process, this CDI was

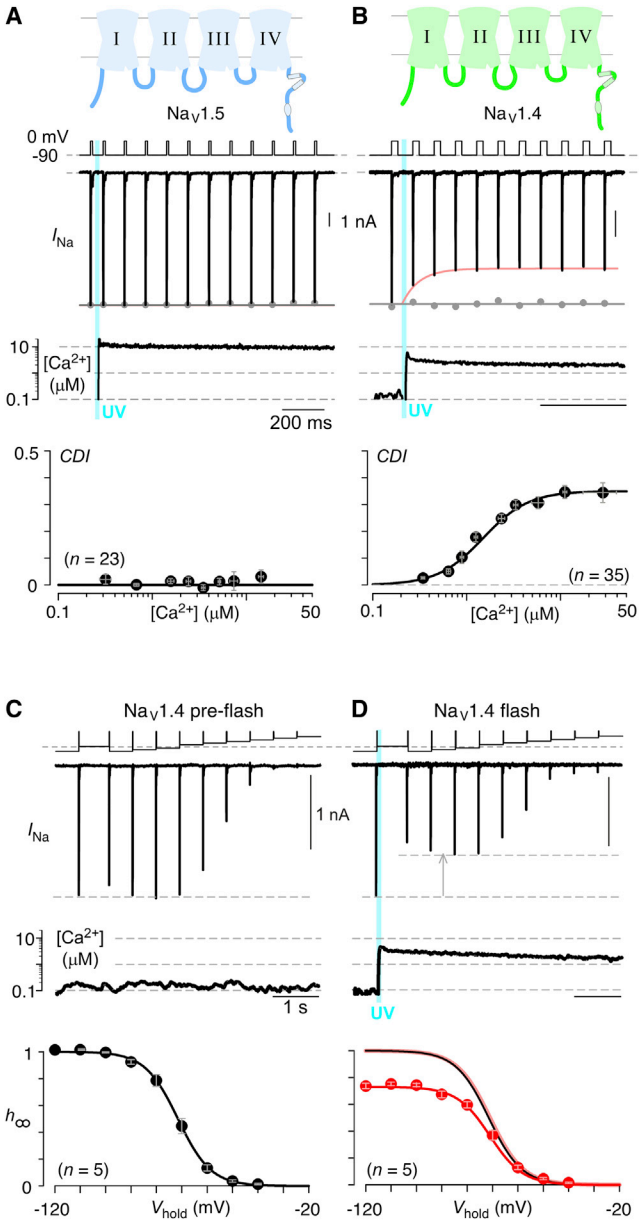

Figure 2. CDI of Na Channels under Ca^{2+} Photouncaging

(A) $Na_V1.5$ currents unaffected by 10 μM Ca^{2+}. Gray dots, peak currents before uncaging. Bottom, mean data for *CDI* versus Ca^{2+}-step amplitude. *CDI* = 1 − average peak I_{Na} of last three to four responses after Ca^{2+} uncaging/peak I_{Na} before uncaging. Symbols, mean ± SEM of ~5 uncaging events compiled from 23 cells. See Figure S2.

(B) $Na_V1.4$ peak currents decline during 2 μM Ca^{2+} step (rose fit). Format as in (A). Bottom, mean *CDI* plotted versus Ca^{2+}. Each symbol, mean ± SEM of ~5 uncaging events compiled from 35 cells. See Figures S2, S3, and S4.

(C) $Na_V1.4$ currents specifying h_∞ at ~100 nM Ca^{2+}. Bottom, h_∞ curve (mean ± SEM, five cells).

(D) Approximately 3 μM Ca^{2+} step uniformly suppresses Na currents. Bottom, corresponding mean h_∞ curve (red symbols and fit), where symbols plot mean ± SEM (five cells). Upwardly scaled h_∞ curve (rose) same as before uncaging (black).

insensitive to pulse rate and voltage, whereas onset kinetics were influenced by Ca^{2+} concentration (Figures S2B–S2D, S3, and S4).

To reconcile these effects on $Na_V1.4$ with those observed under static Ca^{2+} buffering (Figures 1H and S1B), we evoked Na currents under a modified voltage-pulse protocol that measures h_∞ curves just before and after Ca^{2+} uncaging. Prior to Ca^{2+} uncaging, peak currents evoked after various holding potentials demonstrated the usual changes affiliated with steady-state inactivation (Figure 2C, black I_{Na} trace). Normalizing these currents by that of the first pulse yielded a baseline h_∞ curve (Figure 2C, bottom subpanel), here averaged over multiple cells. Figure 2D shows the effect of Ca^{2+} uncaging in same cell. The initial current, obtained just prior to Ca^{2+} uncaging, exhibits the identical amplitude as its analog in Figure 2C, confirming minimal rundown. By contrast, after Ca^{2+} uncaging, the resulting currents (Figure 2D, black I_{Na} trace after UV flash) were uniformly suppressed compared to Figure 2C. Normalizing these responses (after Ca^{2+} uncaging) by that of the first pulse (just before uncaging) yields the Ca^{2+}-regulated h_∞ curve shown below (Figure 2D, bottom subpanel, red data and fit), as averaged over multiple cells. For reference, the fit to the h_∞ curve obtained before Ca^{2+} uncaging is reproduced in black in Figure 2D. Importantly, by scaling up the fit to the h_∞ curve following Ca^{2+} uncaging, we obtain a rose-colored curve that precisely overlays the control relation in black. Hence, Ca^{2+} elevation would have the apparent effect of scaling down the h_∞ curve without shift along the voltage axis, just as seen in Figure 1H. The actual CDI effect reflects decreased channel open probability, separate from fast inactivation, as shown in the next section.

Na Channel Regulation by Ca^{2+} Fluxing through Neighboring Ca^{2+} Channels

We next induced Ca^{2+} regulation of Na channels by more physiological means, so as to exclude unsuspected photouncaging effects that might artifactually produce the results in Figure 2 and to permit observations at the level of single Na channel molecules (impractical in the electrical environment of photouncaging equipment).

Accordingly, $Na_V1.4$ and $Ca_V2.1$ Ca^{2+} channels were coexpressed within the same cells to test whether Ca^{2+} spillover from a Ca^{2+} channel source could inhibit nearby Na channels (Figure 3A). Owing to the higher threshold of voltage activation for $Ca_V2.1$ versus $Na_V1.4$, Na current alone could be evoked by modest depolarizations to 0 mV (Figures S5A–S5C), which bookend the voltage pulse protocol shown in Figure 3B. Na currents (I_{Na}) evoked in this manner have the same magnitude. By contrast, insertion of an intervening 30 mV pulse activates Ca^{2+} currents, as shown by the red shading in Figure 3C. Importantly, the second Na current response is then substantially diminished, as if Ca^{2+} influx through adjacent Ca^{2+} channels triggered Na channel CDI. To exclude voltage-dependent inhibition as the cause of a diminished second response, the intervening voltage pulse was further increased to the Ca^{2+} channel reversal potential (~90 mV), where negligible Ca^{2+} entry would occur. Reassuringly, the second Na response appeared identical to the first (Figure 3D), arguing that the reduction of Na current above (Figure 3C) was due to Ca^{2+} influx and not voltage itself.

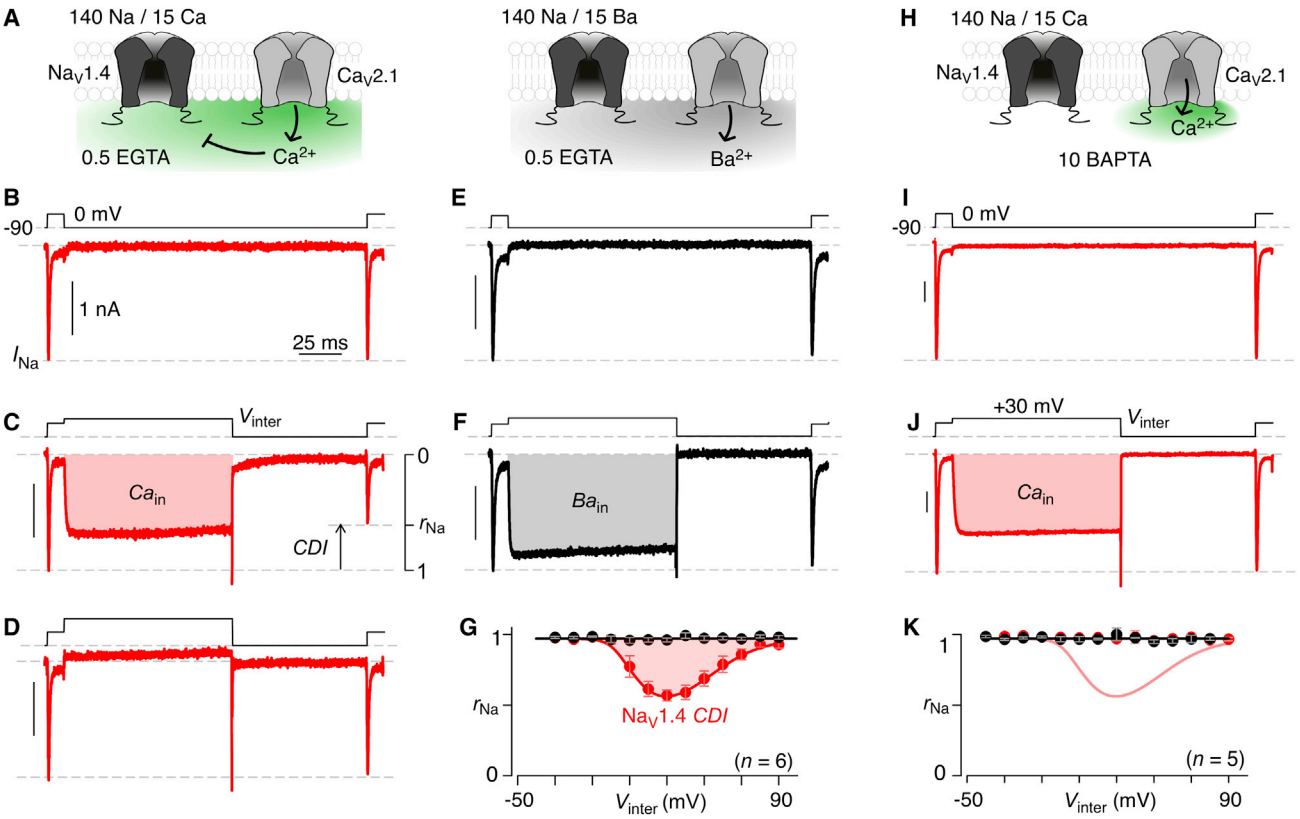

Figure 3. Na Channel Regulated by Ca^{2+} Spillover from Ca^{2+} Channels

(A) Schematic, Ca^{2+} spillover from $Ca_V2.1$ inhibiting Na channels.

(B) Dual voltage pulses selectively evoke identical $Na_V1.4$ currents. See Figure S5.

(C) Intervening +30 mV pulse (V_{inter}) activates $Ca_V2.1$, diminishing ensuing Na current. r_{Na}, fraction of Na current remaining after $Ca_V2.1$ Ca^{2+} influx.

(D) V_{inter} to +90 mV rescues the second $Na_V1.4$ current.

(E and F) Na current amplitude unperturbed by Ba^{2+} influx through $Ca_V2.1$ channels.

(G) Mean relation for r_{Na} versus V_{inter} shows U shape with Ca^{2+} (red), but not Ba^{2+} (black). Symbols, mean ± SEM (six cells).

(H–K) Restricting Ca^{2+} to $Ca_V2.1$ nanodomain prevents Na channel CDI. (K) Symbols, mean ± SEM (five cells), format as in (G). See Figure S5.

Analyzing averaged data for the fraction of current remaining in second versus first Na responses (r_{Na} in Figure 3C) confirms a U-shaped dependence of CDI on intervening pulse potential (Figure 3G, red). Additionally, we examined the effects of substituting Ba^{2+} for Ca^{2+} as charge carrier through Ca^{2+} channels. Because Ba^{2+} binds poorly to CaM (Chao et al., 1984), we expected Na channel CDI to disappear (Figure 3A, right subpanel), as confirmed in Figures 3E–3G (black). As a further test, adding 10 mM BAPTA to the dialyzate eliminated $Na_V1.4$ CDI (Figures 3H–3K and S5D–S5F), demonstrating that Ca^{2+} channel spillover drove the Na channel regulation. Finally, as expected, like experiments with $Na_V1.5$ revealed no CDI (Figures S5G–S5J).

Importantly, this strategy of coexpressing Na and Ca^{2+} channels could be extended from cells to isolated patches of membrane, permitting observations of regulation at the level of individual Na channels, something never before attempted. Figure 4A shows the activity of a patch containing several $Na_V1.4$ channels coexpressed with hundreds of $Ca_V2.1$ Ca^{2+} channels. A multichannel stochastic record is shown at the top (multichannel record), along with the voltage-pulse protocol. Only Na channels were activated during test-pulse depolarizations to −30 mV at the left (labeled i) and right (labeled ii) ends of the record; Ca^{2+} channels were activated only during the interpulse to a more positive voltage of 30 mV (shaded in red). The ensemble average of many such records is shown below. Thus oriented, one can clearly appreciate that Na channel activity evoked after intense interpulse Ca^{2+} entry was substantially decreased (pulse ii), compared to the activity before the interpulse (pulse i). Data from a separate patch containing only $Na_V1.4$ channels without $Ca_V2.1$ channels demonstrate no such difference between first and second test pulses (Figure 4D). Thus, Ca^{2+} entry caused the reduction of second pulse activity in Figure 4A, an effect confirmed in multiple patches, with a mean decrement of current amounting to 45.4% ± 8.8% (mean ± SEM, n = 6).

To distinguish the elementary mechanism of inhibition, we analyzed the unitary current *i* approximated by the horizontal dashed line on the multichannel record (Figure 4A, labeled *i* ~−1 pA). This unitary current was not visibly changed in the second test pulse compared to the first, suggesting that single-channel conductance was unaffected by CDI. This outcome is

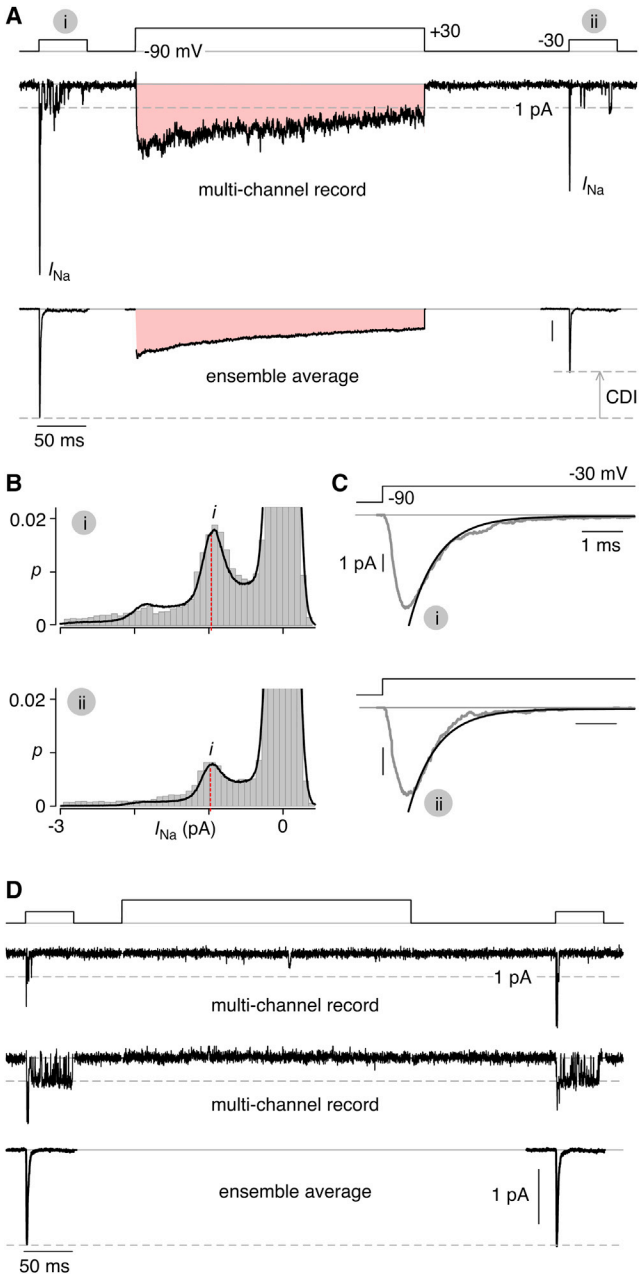

Figure 4. Multichannel Stochastic Records of $Na_V1.4$ CDI

(A) Multichannel records from HEK293 cells coexpressing $Na_V1.4$ and $Ca_V2.1$ channels. On-cell patch configuration. Voltage protocol (top), multichannel record (middle), and ensemble average current (bottom). Red shading, Ca^{2+} entry. Ensemble average shows reduced Na channel activity after Ca^{2+} entry (pulse ii) versus before (pulse i).

(B) Amplitude histogram analysis of patch from (A) shows no change in unitary current following Ca^{2+} entry (top before interpulse; bottom after interpulse). Amplitude histogram analysis of events occurring 0.5–17 ms after pulse onset during −30 mV test pulses. Fits (black) to data (gray) derived from amplitude analysis of low-pass filtered stochastic channel simulations with added Gaussian noise. Dashed red lines, unitary current *i* used to generate fits.

(C) Expanded time base display of ensemble average currents from (A) before (top) and after (bottom) Ca^{2+}. Fast inactivation is essentially identical; same time constant for both monoexponential fits (black curves).

(D) Multichannel stochastic records of separate patch with only $Na_V1.4$ channels. No difference in channel activity before and after intervening pulse (mean decrement ~0.2% ± 3%; mean ± SEM, n = 5 patches). Second multichannel record chosen to illustrate rare occurrence of persistent gating mode. Format as in (A).

explicitly confirmed in Figure 4B by amplitude histogram analysis, where the smooth curve fit to data (in black) is generated by stochastic simulation of multichannel activity added to Gaussian noise, followed by low-pass filtering present in our system (Prod'hom et al., 1987). Using this method, essentially the same underlying value of *i* was estimated before and after CDI (vertical red dashed lines). Accordingly, because ensemble average current $I = N P_O i$, and the number of channels *N* must be the same in first and second test pulses (separated by only hundreds of milliseconds), CDI must occur by decreased open probability P_O, just as in Ca^{2+} channel CDI (Imredy and Yue, 1994). To exclude appreciable interaction of the CDI-mediated decrease in open probability with fast inactivation, we confirmed that the time constant of inactivation was not detectably changed by CDI (Figure 4C), echoing whole-cell results in Figure S2B. Thus, CDI and fast inactivation are largely parallel processes.

In all, we emphasize that the whole-cell functional profile in Figure 3G (both Ca^{2+} and Ba^{2+} relations) resembles that for Ca^{2+} channels (Figure 1C) and recapitulates the classic engram of native Ca^{2+} regulation of Ca^{2+} channels historically established by Eckert and colleagues (Eckert and Chad, 1984). Additionally, the single-channel behavior in Figure 3A closely mirrors that observed for native single Ca^{2+} channels (Imredy and Yue, 1994). Therefore, from the functional standpoint, the Ca^{2+} regulation of $Na_V1.4$ channels notably resembles that of Ca^{2+} channels.

N-Terminal Lobe of CaM as Ca^{2+} Sensor

With robust functional resolution of Na channel Ca^{2+} regulation in hand, we could appropriately seek after its mechanistic underpinnings, searching first for the Ca^{2+} sensor of $Na_V1.4$ modulation. Prior work has argued that the first vestigial EF hand in the CI region binds Ca^{2+} and triggers modulation (Biswas et al., 2009; Shah et al., 2006; Tan et al., 2002; Wingo et al., 2004). We therefore introduced alanines at two potential Ca^{2+}-coordinating residues in the first EF hand of $Na_V1.4$ channels (Figure 1A, "putative Ca binding loops"). If this EF hand were to bind Ca^{2+}, introducing these alanines would reduce Ca^{2+} affinity by 10- to 1,000-fold (Linse and Forsén, 1995). However, this mutant channel still exhibited rapid and strong CDI, indistinguishable from wild-type (Figure 5A), as shown by overlaying the wild-type profile (gray) on the *CDI* –[Ca^{2+}] relation. Other mutations historically proposed to disrupt potential Ca^{2+} binding to this EF hand also spared CDI (Figures S6A–S6C). Thus, this EF hand motif is not the Ca^{2+} sensor for CDI, paralleling outcomes in Ca^{2+} channels (Peterson et al., 2000; Zhou et al., 1997).

Ca^{2+} binding to a resident CaM serves as the primary Ca^{2+}-sensing event in the regulation of Ca^{2+} channels (Peterson et al., 1999; Zühlke et al., 1999). Likewise, some studies of Na channels have argued that CaM may be at least one of the pertinent Ca^{2+} sensors, based on biochemical and structural

inferences (Kim et al., 2004a; Sarhan et al., 2012). Crucially lacking, however, has been a key result seen with Ca^{2+} channels coexpressed with a dominant-negative mutant CaM (CaM_{1234}), where Ca^{2+} binding has been severely attenuated by alanine substitutions into all its EF hands. Importantly, coexpressing CaM_{1234} with Ca^{2+} channels fully abolishes their Ca^{2+} regulation, arguing clearly for CaM as the Ca^{2+} sensor (Peterson et al., 1999; Zühlke et al., 1999). By contrast, no prior Na channel study has demonstrated elimination of Ca^{2+} regulation by CaM_{1234}. Rather, the effects have been variable and inconsistent (Van Petegem et al., 2012).

Here, however, we observed a notably straightforward result upon coexpressing $Na_V1.4$ channels with CaM_{1234}. Figure 5B demonstrates total suppression of CDI, a result advocating strongly that CaM is the primary Ca^{2+} sensor for Na channels. Reassuringly, coexpression of CaM_{1234} also suppressed $Na_V1.4$ CDI observed by Ca^{2+} fluxing through neighboring Ca^{2+} channels (Figures S6D and S6E). Additionally, the strong actions of CaM_{1234} permitted higher-order tests whether one lobe of CaM or the other suffices to trigger Na channel regulation. Such single-lobe signaling would add to the ranks of a functional bipartition paradigm (Preston et al., 1991), richly observed throughout the Ca^{2+} channel superfamily (DeMaria et al., 2001; Liang et al., 2003; Peterson et al., 1999; Yang et al., 2006). In this regard, we utilized a mutant CaM_{12} construct, featuring selective inhibition of Ca^{2+} binding to the N, but not C, lobe. Coexpressing $Na_V1.4$ channels with CaM_{12} also fully abolished Ca^{2+} regulation (Figure 5C), arguing that Ca^{2+} binding to the N lobe is necessary for CDI. Alternatively, coexpressing $Na_V1.4$ channels with CaM_{34} (selective inhibition of Ca^{2+} binding to C lobe) entirely preserved CDI (Figure 5D), with a profile nearly indistinguishable from control (reproduced as gray). Thus, Ca^{2+} binding to the N lobe of CaM is both necessary and sufficient to trigger Na channel CDI. Indeed, the two Ca^{2+}-binding sites within the critical N lobe fit well with the Hill steepness coefficient of 1.8 observed in *CDI* –[Ca^{2+}] relations (Linse and Forsén, 1995). We note that our result contrasts with a prior proposal that Ca^{2+} binding to C lobe triggers regulation of Na channels (Sarhan et al., 2012; Van Petegem et al., 2012). As a final check for the predominance of CaM as Ca^{2+} sensor, we demonstrated that CaM kinase II inhibition had no effect on Na channel CDI (Figures S6F and S6G).

Structural Determinants of Na Channel Ca^{2+} Regulation

The CI region of Ca^{2+} channels (Figure 1A) suffices to confer Ca^{2+} regulation (de Leon et al., 1995). Yet, prior work in Na channels emphasizes the necessary role of the III-IV loop, a critical determinant for fast inactivation of these channels (Stühmer et al., 1989). A recent crystal structure of Ca^{2+}/CaM complexed with the III-IV loop of $Na_V1.5$ channels further suggests that a conserved tyrosine anchor is necessary for Ca^{2+}/CaM binding and that this binding is required for Ca^{2+} modulation (Sarhan et al., 2012; Van Petegem et al., 2012). Figure S7A contextualizes the location of this anchor in relation to other Na channel landmarks.

Accordingly, we substituted alanine for the homologous tyrosine in $Na_V1.4$ channels (Y[1311]A) and tested for Ca^{2+} regulation. In contrast to prior work, we observed that Ca^{2+} regulation was fully present (Figure 5E), with a functional profile indistinguishable from that of wild-type channels. Indeed, disruption of a similar Ca^{2+}/CaM binding site in the III-IV loop of Ca^{2+} channels also failed to disrupt CDI (Figures S7B and S7C). Thus, both Na and Ca^{2+} channels do not require Ca^{2+}/CaM binding to the III-IV loop for Ca^{2+} regulation.

To explore the role of the Na channel CI region in supporting Ca^{2+} regulation, we undertook a convenient chimeric-channel approach, exploiting the lack of Ca^{2+} regulation in $Na_V1.5$ versus $Na_V1.4$. When the carboxy terminus of $Na_V1.4$ was substituted with its Nav1.5 counterpart, Ca^{2+} regulation was completely eliminated (Figure 5F). Yet more telling were the effects of limited mutations within the IQ element (Figure 1A, blue shaded zone), which potently alter Ca^{2+} regulation of Ca^{2+} channels (Bazzazi et al., 2013; Ben Johny et al., 2013; DeMaria et al., 2001; Liang et al., 2003; Yang et al., 2006; Zühlke et al., 1999). When dual alanines were substituted for contiguous isoleucine and glutamine residues in the center of the $Na_V1.4$ IQ element, the Ca^{2+}-dependent inhibition of these channels was not merely eliminated but converted into outright facilitation (CDF, Figure 5G). This effect is eerily similar to that observed upon analogous mutagenesis of certain L-type Ca^{2+} channels (Zühlke et al., 1999, 2000). Finally, fitting with the preeminence of the CI region, binding of Ca^{2+}-free CaM (apoCaM) to the carboxy tail of $Na_V1.4$ channels has been confirmed (Ben Johny et al., 2012).

In all, like Ca^{2+} channels, the carboxy tail of Na channels contains the needed structural determinants for CDI, even regarding inversion of regulatory polarity by like mutations therein.

Ca^{2+} Regulation of Native Na Channels

Encouraged by the recombinant channel findings thus far, we tested for Ca^{2+} regulation in their native counterparts. Though recombinant $Na_V1.5$ channels were not Ca^{2+} regulated, cardiac myocytes might furnish added critical auxiliary factors. Thus, we performed Ca^{2+} uncaging in adult guinea pig ventricular myocytes, where $Na_V1.5$ channels convey the bulk of native Na current. Even here, however, no Ca^{2+} regulation of Na current was observed (Figure 6A).

By contrast, when testing for Ca^{2+} regulation of native $Na_V1.4$ channels in skeletal myotubes derived from mouse GLT cells, we observed robust Ca^{2+} regulation of Na current (Figure 6B), with Ca^{2+} sensitivity appropriate for physiological Ca^{2+} transients (Wagner and Maier, 2006). This result may be the first direct demonstration of Ca^{2+} regulation of endogenous Na currents.

Of further biological concern, channelopathic mutations occur in the carboxy terminus of Na channels, but the alterations in channel function that underlie pathogenesis have not been fully resolved. Might these mutations affect the Ca^{2+} regulation in $Na_V1.4$ channels? Figures 6C and 6D investigate this possibility for channelopathic mutations associated with K- and cold-aggravated myotonias (Kubota et al., 2009; Wu et al., 2005). In both instances, Ca^{2+} regulation is substantially diminished (but see Biswas et al., 2013), whereas the kinetics of currents remain unchanged by Ca^{2+} elevation (Figures S7D and S7E). These results offer previously unrecognized dimensions by which Na channel function may influence disease development.

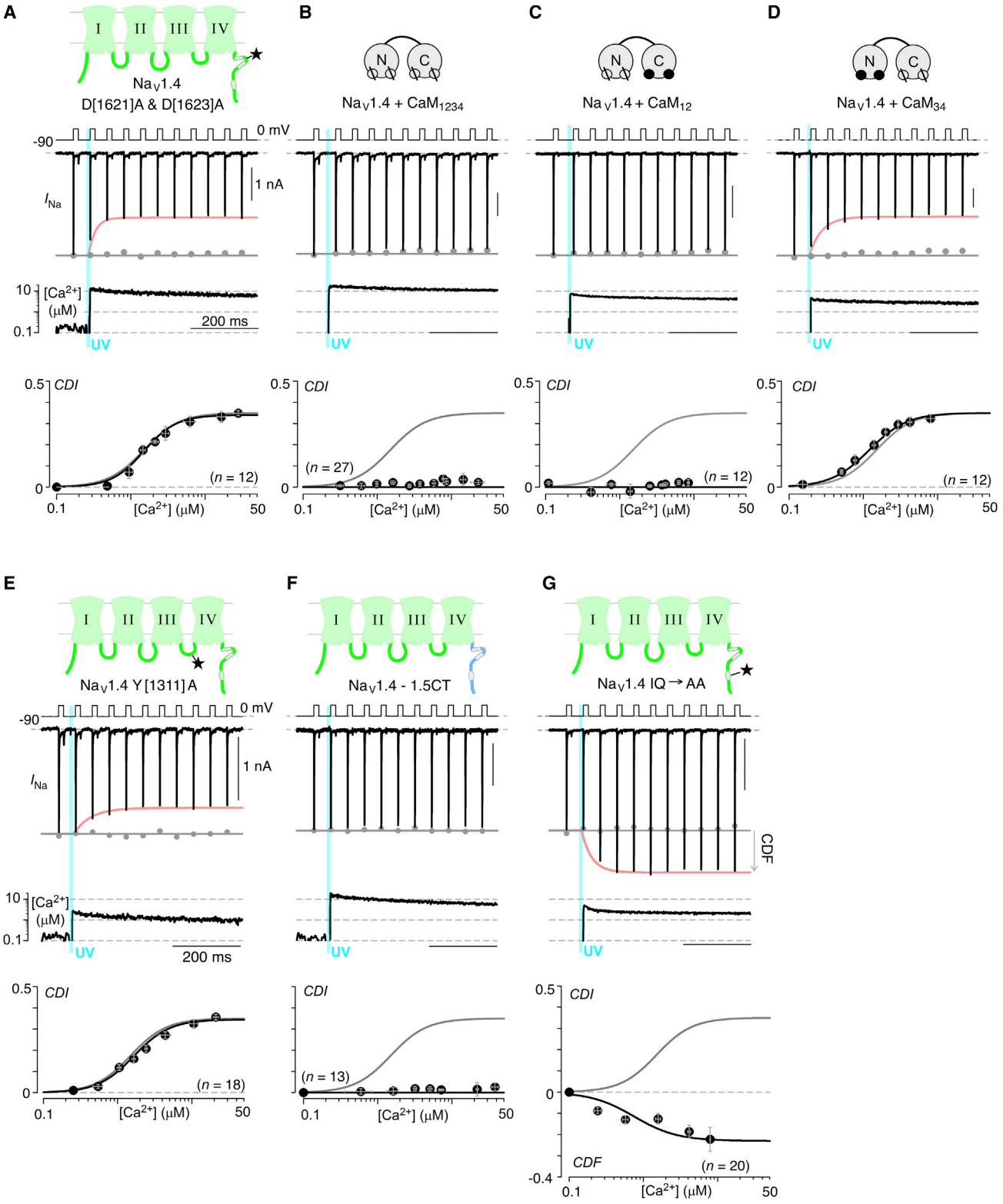

Figure 5. Calmodulin as Ca^{2+} Sensor for $Na_V1.4$ CDI

(A) Mutating putative Ca^{2+}-coordinating residues in $Na_V1.4$ EF hand did not alter *CDI*. Format as in Figure 2B. Symbols, mean ± SEM of ~3 uncaging events from 12 cells.

(B) CaM_{1234} abolishes CDI. Symbols, mean ± SEM (~6 uncaging events from 27 cells).

(legend continued on next page)

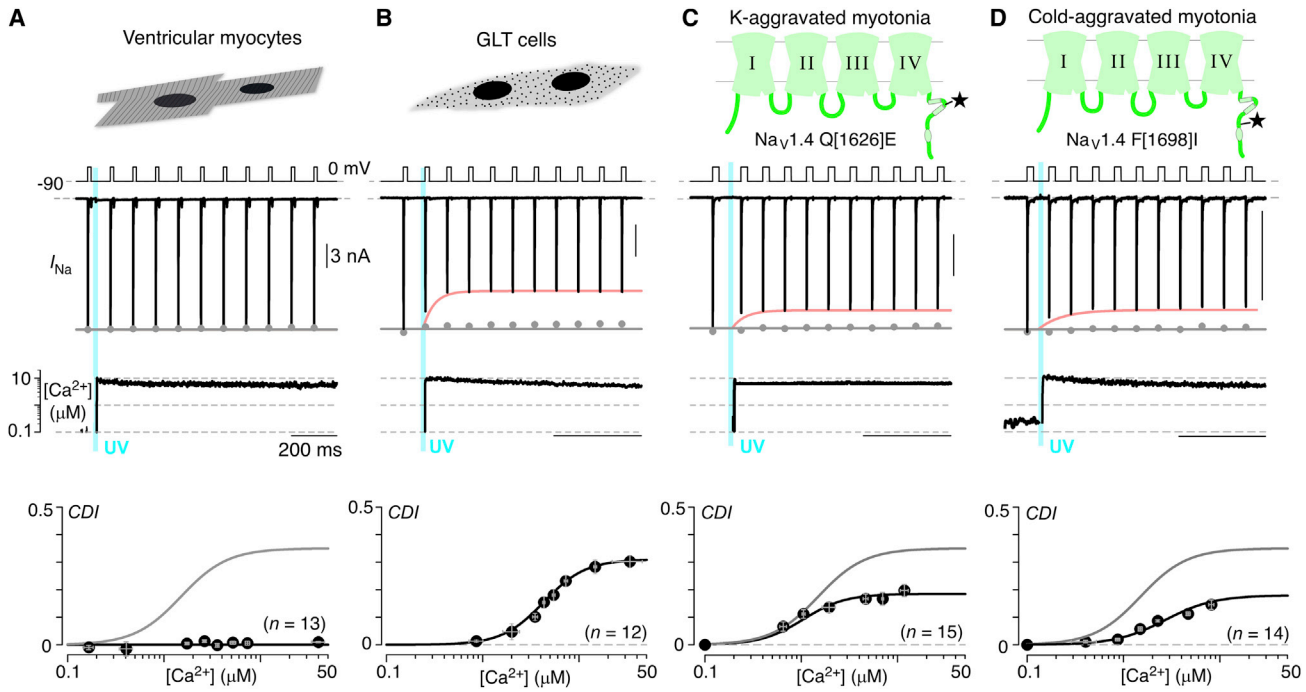

Figure 6. Physiology of Na Channel Ca^{2+} Regulation

(A) No Ca^{2+} regulation of native $Na_V1.5$ in ventricular myocytes. Format as in Figure 2A. Symbols, mean ± SEM from five to six uncaging events (13 cells).

(B) Endogenous $Na_V1.4$ channels in GLT cells exhibit CDI. Minimal contamination by Ca^{2+}-activated Cl current (<5% of I_{Na}) subtracted. Each symbol, mean ± SEM from four to five uncaging events (12 cells).

(C and D) Recombinant $Na_V1.4$ channels with mutations for K- and cold-aggravated myotonias show weaker CDI. Symbols, mean ± SEM from approximately nine uncaging events (indicated number of cells).

DISCUSSION

By applying rapid Ca^{2+} delivery to Na channels (photouncaging of Ca^{2+} and Ca^{2+} spillover from neighboring Ca^{2+} channels), this study significantly refines our understanding of Na channel regulation by Ca^{2+}. First, most prior mechanistic deductions are based on observations on recombinant cardiac Na channels ($Na_V1.5$), and these deductions have suggested that Ca^{2+} regulation of Na channels differs at the core from that in Ca^{2+} channels (Van Petegem et al., 2012). However, by using rapid Ca^{2+} delivery, our experiments detect no Ca^{2+} modulation of either recombinant $Na_V1.5$ channels or their native counterparts in cardiac myocytes. This outcome raises questions about prior structure-function deductions (Biswas et al., 2009; Potet et al., 2009; Sarhan et al., 2012; Shah et al., 2006; Tan et al., 2002; Wingo et al., 2004) and may spur revision to the present understanding of Ca^{2+} regulation in Na channels. Second, more important results concern skeletal-muscle $Na_V1.4$ channels, reputed for only modest Ca^{2+} regulation via mechanisms that diverge significantly from Ca^{2+} channels. Here, rapid Ca^{2+} delivery instead unveils conspicuous Ca^{2+} regulation of $Na_V1.4$ channels. In like manner, the methods are now at hand to explore potential Ca^{2+} regulation of the many other Na channel isoforms ($Na_V1.1$–$Na_V1.9$). Third, we argue for the persistence of a common Ca^{2+} regulatory module across Ca^{2+} and Na channels. In particular, the function and mechanism of Ca^{2+} regulation of $Na_V1.4$ channels bear remarkable similarity to that of Ca^{2+} channels. This long-sought commonality suggests that kindred carboxy-tail Ca^{2+} regulatory modules persist across Ca^{2+} and Na channels, affording common principles for understanding. Indeed, this persistence can be shown as a latent capability within cardiac $Na_V1.5$ channels by substituting the $Na_V1.4$ carboxy tail onto the $Na_V1.5$ backbone (Figure 7A). This maneuver confers Ca^{2+} regulation to the resulting chimeric channels, with Ca^{2+} sensitivity akin to that of $Na_V1.4$ (gray trace). Of greater generality, carboxy-tail transplantation between Ca^{2+} and Na channels (shown below) fully establishes the carboxy-tail domain as a legitimate module across superfamilies. Finally, channelopathic

(C) Eliminating N-lobe Ca^{2+} binding (CaM_{12}) abolishes CDI. Symbols, mean ± SEM of 4 to 5 uncaging events from 12 cells.

(D) Eliminating C-lobe Ca^{2+} binding (CaM_{34}) spares CDI. Symbols, mean ± SEM of ~5 uncaging events from 12 cells.

(E) Mutating $Na_V1.4$ III-IV loop spares CDI. Format as in Figure 2B. Symbols, mean ± SEM of 4 to 5 uncaging events from 18 cells.

(F) No CDI in $Na_V1.4$-1.5CT chimera. Symbols, mean ± SEM of 4 to 5 uncaging events (13 cells).

(G) Substituting dual alanines for key isoleucine-glutamine residues in $Na_V1.4$ IQ domain yields facilitating Na currents. Bottom, mean data confirm facilitation, shown as negative *CDI*. Symbols, mean ± SEM of ~13 uncaging events (20 cells).

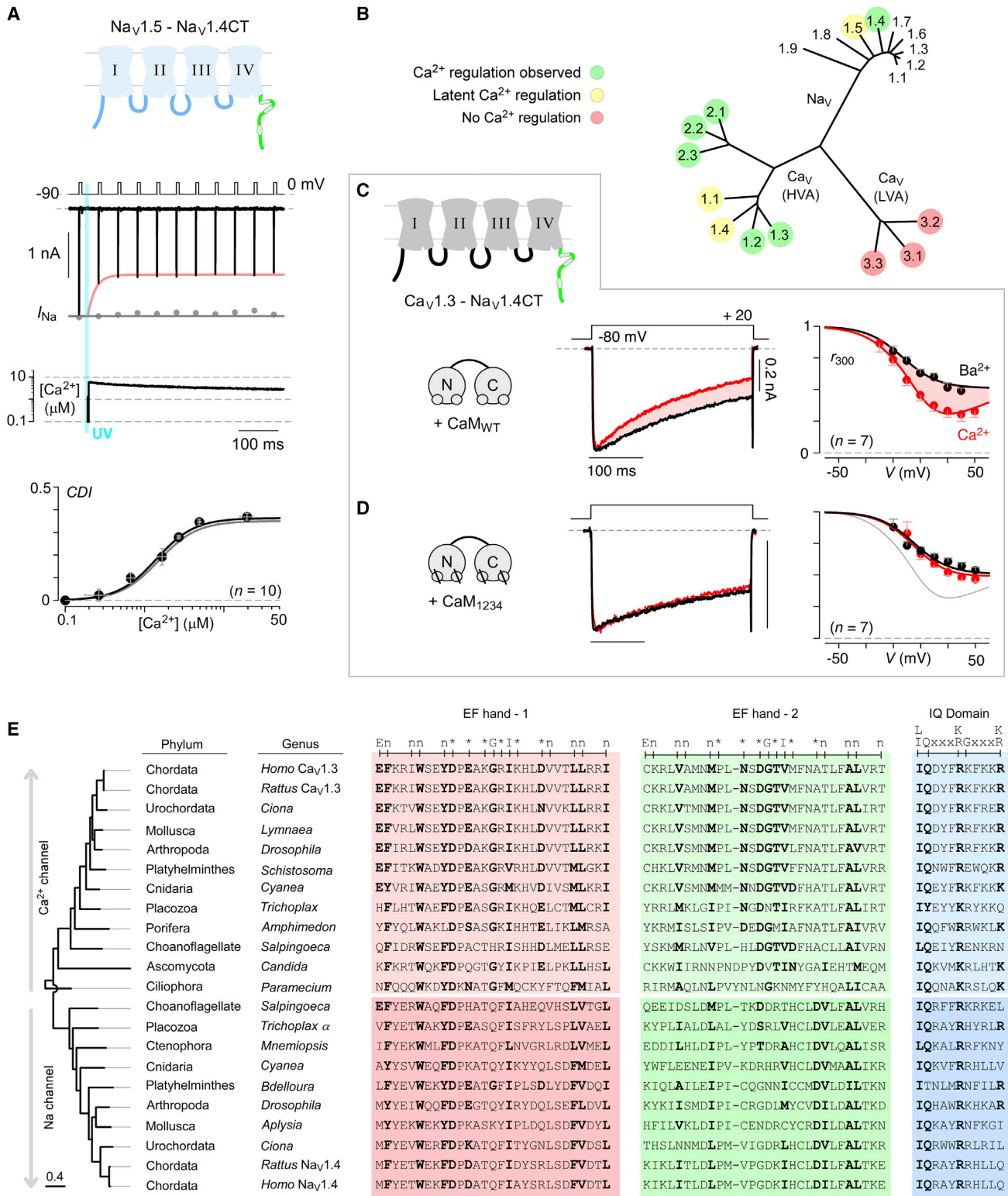

Figure 7. Persistence of CaM/CI Module across Na and Ca^{2+} Channel Superfamilies

(A) Transferring Na$_V$1.4 carboxy tail to Na$_V$1.5 backbone (Na$_V$1.5-1.4CT) confers latent Ca^{2+} regulation (wild-type Na$_V$1.4, gray fit in bottom subpanel). Format as in Figure 2A. Symbols, mean ± SEM from four to five uncaging events (ten cells).

(B) Phylogenetic tree of the Na and Ca^{2+} channel superfamilies.

(legend continued on next page)

mutations for cold- and K-aggravated myotonias halve the Ca^{2+} regulation of $Na_V1.4$, and Ca^{2+} regulation of native skeletal Na currents is observed. The carboxy tail of Na channels now looms as a molecular target for these myotonias and related diseases.

Prior Na Channel Studies of Ca^{2+} Regulation

Before turning to the implications of newly observed forms of Ca^{2+} regulation, we consider potential explanations for prior observations of Ca^{2+}-dependent shifts in steady-state inactivation curves (i.e., h_∞ curves in Figure 1E). Most mechanistic postulates regarding Ca^{2+} regulation of Na channels are based on such shifts (summarized in the Introduction). One can note that the Ca^{2+} chelators EGTA and BAPTA were used to nominally buffer free Ca^{2+} concentrations at levels substantially higher than the dissociation constants for these compounds. If Ca^{2+} concentrations were to far exceed 10 μM, it would be difficult to undertake whole-cell patch clamp. It is then understandable that most have resorted to intracellular solutions with CsF, which greatly facilitates recording but indiscriminately activates G protein signaling (Sternweis and Gilman, 1982), among numerous other effects (Van Petegem et al., 2012). Moreover, before measurements are taken, time-dependent voltage shifts in h_∞ curves are typically allowed to equilibrate following the onset of whole-cell pipet dialysis (Biswas et al., 2009). Ambiguities about actual equilibration may then contribute to conflicts among prior reports. Importantly, the present study does document a lack of Ca^{2+}-dependent shift in h_∞ curves using two approaches: static measurements that employ HEDTA to buffer Ca^{2+} at levels close to the corresponding dissociation constant and rapid photouncaging of Ca^{2+} with concurrent readouts of Ca^{2+}. Thus, the difference in results about voltage shifts in h_∞ relations merits ongoing attention in the field.

Open Frontier for Other Na Channel Isoforms

That said, it is clear that, by using Ca^{2+} photouncaging or Ca^{2+} influx via neighboring Ca^{2+} channels, one can now resolve Ca^{2+} regulation of $Na_V1.4$ channels that is more rapid, robust, and similar to Ca^{2+} channels than could be previously observed. Likewise, the means of Ca^{2+} delivery used here may facilitate characterization of other superfamily members (Figure 7B, $Na_V1.1$–$Na_V1.9$, except $Na_V1.5$), all possessing high carboxy-tail homology. Many Ca^{2+} channels exhibit variant forms of CaM regulation, where the precise functional behavior can differ; for example, Ca^{2+} facilitates opening of $Ca_V2.1$ channels (DeMaria et al., 2001; Lee et al., 1999) but produces CDI in $Ca_V1.3$ (Figure 1C). Although we have here investigated the best-studied $Na_V1.4$ and $Na_V1.5$ channels, it will be interesting to explore other Na channels for various forms of Ca^{2+} regulation. In all, there is the potential for Ca^{2+} regulation across the Na channel superfamily by an array of Ca^{2+} sources like voltage-gated Ca^{2+} channels, ryanodine and IP3 channels, Ca^{2+}-permeable AMPA and NMDA receptors, and store-operated Ca^{2+} channels (Berridge, 2012).

Synergistic Study of Na and Ca^{2+} Channels

Given the parallels between Ca^{2+} regulation in Na and Ca^{2+} channels, we attempted a further, patently simple test for the persistence of a common CaM-CI regulatory element among Ca^{2+} and Na channels—the transplantation of the Ca^{2+}-inactivating (CI) module from one superfamily to another. On adjoining the core of a $Ca_V1.3$ channel to the carboxy tail of $Na_V1.4$ (Figure 7C), not only were sizeable currents expressed, but also the faster decay of Ca^{2+} versus Ba^{2+} currents (top), according to a classic profile (r_{300} plot below), indicates Ca^{2+} regulation (CDI) in this chimera (cf., Figure 1C). Importantly, coexpressing mutant CaM_{1234} abolishes this CDI (Figure 7D), just as in $Na_V1.4$ (Figure 5B). Hence, the regulatory design of one superfamily persists with sufficient congruity to functionally interface with the core of another. This modularity may rival that of voltage-paddle elements transferable from Na_V to K_V channels (Bosmans et al., 2008).

Thus established, the commonality of the CaM-CI module promises insights from synergistic coinvestigation of Na and Ca^{2+} channels. Structural biological efforts with Na channels have arguably overtaken those with Ca^{2+} channels, given the atomic resolution of nearly intact Na channel CI domains complexed with CaM (Wang et al., 2012). Though results from the present study may spur reinterpretation of inferences drawn from these structures, Na channel structures like these can now be viewed as holding potentially adaptable lessons for Ca^{2+} channels. In particular, recent advances suggest that Ca^{2+} channel CDI arises from a tripartite complex of the channel EF hand segment, the IQ domain, and a single lobe of CaM (Ben Johny et al., 2013). Emerging Na channel structures may comment on this proposal and whether this Ca^{2+} channel scheme extends in some form to Na channels.

Antiquity of CaM-CI Module

More general implications concern the antiquity of the CaM-CI Ca^{2+} regulatory module. Figure 7B depicts the phylogenetic tree of Na and Ca^{2+} channel superfamilies based on carboxy-tail sequences. The CI region is conserved across the top branches of this tree, conferring Ca^{2+} regulation to certain Na and Ca^{2+} channels (Ca_V1 and Ca_V2 branches). To further explore historical lineage, we undertake CI sequence alignment and phylogenetic analysis of Ca^{2+} and Na channels from multiple eukaryotic phyla (Figure 7E), starting with *Paramecium*. This single-cell organism lacks voltage-gated Na channels but possesses a Ca^{2+} channel in which Ca^{2+} regulation was first discovered (Brehm and Eckert, 1978). From this start, the Ca^{2+} channel clade for more advanced organisms branches toward the top, and the Na channel clade branches toward the bottom. CI

(C) Transplanting $Na_V1.4$ carboxy tail onto $Ca_V1.3$ backbone ($Ca_V1.3$-$Na_V1.4$CT) yields chimeric channel that retains Ca^{2+} regulation. Format as in Figure 1C. Symbols, mean ± SEM, seven cells. CDI measured under low Ca^{2+} buffering (see Extended Experimental Procedures).

(D) Coexpressimg CaM_{1234} with $Ca_V1.3$-$Na_V1.4$CT abolishes CDI. Format as in Figure 1C. Symbols, mean ± SEM, seven cells. CDI measured as in (C).

(E) Maximum likelihood phylogenetic tree shows conservation among Ca^{2+} and Na channel CI regions, across major eukaryotic phyla. Format as in Figure 1A. Consensus sequence patterns for motifs on top. Sequence alignment starts at the center with the *Paramecium* Ca^{2+} channel. Ca^{2+} channels from progressively more advanced organisms branch to the top (pale colors), and those for Na channels branch to the bottom (darker colors).

sequence similarity is conserved throughout. Given this common heritage dating to early eukaryotes (~1 billion years ago), we suggest a persistent link between modern CI elements of Ca^{2+} and Na channels to a primeval Ca^{2+} modulatory design.

CaM-CI Elements as Potential Molecular Therapeutic Targets

Finally, two results are notable from the disease perspective—channelopathic mutations for cold- and K-aggravated myotonias halve the Ca^{2+} regulation of $Na_V1.4$ channels and the direct demonstration of such modulation in skeletal myotubes. Na channel CDI may thus play a physiological role in activity-dependent feedback control of skeletal-muscle excitability. This CDI might normally raise the threshold for muscle excitation during repetitive activity, protecting against overexcitability caused by rapidly elevating extracellular K levels during contraction (Clausen, 2011). Weakening of CDI by channelopathic mutations may predispose for debilitating myotonias (Cannon, 1997). More broadly, CDI mediated by CaM-CI elements in Ca^{2+} channels control cardiac action potential duration (Alseikhan et al., 2002; Mahajan et al., 2008), whose dysregulation predisposes for long QT syndrome and life-threatening arrhythmias (Crotti et al., 2013; Limpitikul et al., 2014). Moreover, numerous channelopathies relate to mutations within the CI regions of Na and Ca^{2+} channels, and these conditions model diseases of more general prevalence (Adams and Snutch, 2007; Kubota et al., 2009; Zimmer and Surber, 2008). As such, the CaM-CI elements of Na and Ca^{2+} channels now present as potential molecular therapeutic targets for certain myotonias, cardiac arrhythmias, and other diseases. A collective view of these conditions as perturbations of CaM-CI function may offer fresh insights into pathogenesis and unified screens for small-molecule therapies.

EXPERIMENTAL PROCEDURES

Molecular Biology

The rat $Na_V1.4$ channel (Trimmer et al., 1990) was cloned in pcDNA3 (Invitrogen) via flanking EcoRI sites. The carboxy-tail sequence agrees with clone *Y17153.1* (GenBank). Human $Na_V1.5$ corresponds to clone *M77235.1* (GenBank). The $Ca_V1.3$ construct $\alpha_{1D}\Delta1626$ was engineered from rat brain variant *AF370009* (GenBank), as described (Ben Johny et al., 2013). Construction of chimeras and mutants is detailed in the Supplemental Information.

Whole-Cell Recording

Whole-cell recordings were obtained at room temperature (~298 K) with an Axopatch 200A amplifier (Axon Instruments). Electrodes were made of borosilicate glass (World Precision Instruments, MTW 150-F4), yielding pipets of 1–2 MΩ resistance, which was compensated by >70%. Pipets were fabricated with a horizontal micropipette puller (model P-97, Sutter Instruments) and fire polished with a microforge (Narishige). Data acquisition utilized an ITC-18 (Instrutech) data acquisition unit controlled by custom MATLAB software (Mathworks). Currents were low-pass filtered at 5 kHz before digitization at several times that frequency. P/8 leak subtraction was used. For Ca^{2+} uncaging, $Na_V1.4$ channels were repetitively pulsed to 0 mV for 15 ms during a 20 Hz train, with 30 s rest intervals between trains. Holding potential was −90 mV unless otherwise noted. For GLT cell experiments, the same protocol was used, except pulses to 0 mV lasted 10 ms. For $Na_V1.5$ experiments (including ventricular myocytes in Figure 6A), pulses to 0 mV for 15 ms were presented as 10 Hz trains punctuated by 30 s rest intervals. Holding potential was also −90 mV unless otherwise noted. Further details are provided in the Supplemental Information.

Single-Channel Recording

All multichannel records were obtained in the on-cell configuration with HEK293 cells (Figure 4). Data were acquired at room temperature using the integrating mode of an Axopatch 200A amplifier (Axon Instruments). Patch pipettes (4–15 MΩ) were pulled from ultra-thick-walled borosilicate glass (BF200-116-10; Sutter Instruments) using horizontal puller (P-97, Sutter Instruments), fire polished with a microforge (Narishige), and coated with Sylgard (Dow Corning). Elementary currents were low-pass filtered at 5 kHz with a four-pole Bessel filter and digitized at 200 kHz with an ITC-18 unit (Instrutech), controlled by custom MATLAB software (Mathworks). Leak subtraction and analysis were previously described (Imredy and Yue, 1992).

Ca^{2+} Uncaging and Fluorescence Measurements

Ca^{2+}-uncaging experiments used a Nikon TE2000 inverted microscope with Plan Fluor Apo 40× oil objective. Ca^{2+} was uncaged by ~1.5 ms duration UV flashes (Cairn UV photolysis system). Flashes driven by discharge of 4,000 μF capacitor bank charged to 200–300 V. PMTs were shuttered during UV pulse to prevent photodamage. For Ca^{2+} imaging, Fluo4FF and Alexa568 dyes (in fixed ratios) were dialyzed into cells and imaged with Argon laser excitation (514 nm). Autofluorescence of each cell was obtained before pipet dialysis. Single-cell fluorescence emission was isolated by field-stop aperture. Dual-color fluorescence emission was obtained with 545DCLP dichroic mirror paired with a 545/40BP filter for Fluo4FF and 580LP filter for Alexa568. Uncaging was conducted after ~2 min dialysis. Steady-state [Ca^{2+}] measured 150 ms after uncaging.

SUPPLEMENTAL INFORMATION

Supplemental Information includes Extended Experimental Procedures and seven figures and can be found with this article online at http://dx.doi.org/10.1016/j.cell.2014.04.035.

AUTHOR CONTRIBUTIONS

M.B.-J. created mutant channels, performed electrophysiology, conducted flash photolysis experiments, and undertook extensive data analysis. P.S.Y. created mutant Ca^{2+} channels and performed experiments relating to the potential role of the III-IV loop in mediating Ca^{2+} channel CDI. M.B.-J. and D.T.Y. conceived the project, refined experimental design and hypotheses, and wrote the paper. J.N. and W.Y. established the GLT cell culture system. R.J.-M. generously provided high-quality adult guinea pig ventricular myocytes.

ACKNOWLEDGMENTS

We thank Gordon Tomaselli, King-Wai Yau, Paul Adams, and members of the Ca^{2+} signals lab for comments. Michael Tadross helped construct and advised on the use of the flash photolysis setup. We thank Dr. Yi Chen-Izu for the generous loan of a flash photolysis system and Drs. Manfred Grabner and Bernhard Flucher for GLT cells. This work was supported by grants from the NINDS (to D.T.Y.) and NIMH (M.B.J.).

Received: February 14, 2014
Revised: March 25, 2014
Accepted: April 15, 2014
Published: June 19, 2014

REFERENCES

Adams, P.J., and Snutch, T.P. (2007). Calcium channelopathies: voltage-gated calcium channels. Subcell. Biochem. *45*, 215–251.

Alseikhan, B.A., DeMaria, C.D., Colecraft, H.M., and Yue, D.T. (2002). Engineered calmodulins reveal the unexpected eminence of Ca^{2+} channel inactivation in controlling heart excitation. Proc. Natl. Acad. Sci. USA *99*, 17185–17190.

Babitch, J. (1990). Channel hands. Nature *346*, 321–322.

Bazzazi, H., Ben Johny, M., Adams, P.J., Soong, T.W., and Yue, D.T. (2013). Continuously tunable Ca(2+) regulation of RNA-edited CaV1.3 channels. Cell Rep. *5*, 367–377.

Ben Johny, M., Yue, D.N., and Yue, D.T. (2012). A novel FRET-based assay reveals 1:1 stoichiometry of apocalmodulin binding across voltage-gated Ca and Na ion channels. Biophys J. *102*, 125a–126a.

Ben Johny, M., Yang, P.S., Bazzazi, H., and Yue, D.T. (2013). Dynamic switching of calmodulin interactions underlies Ca2+ regulation of CaV1.3 channels. Nature Commun. *4*, 1717.

Berridge, M.J. (2012). Calcium signalling remodelling and disease. Biochem. Soc. Trans. *40*, 297–309.

Bers, D.M., Patton, C.W., and Nuccitelli, R. (2010). A practical guide to the preparation of Ca(2+) buffers. Methods Cell Biol. *99*, 1–26.

Biswas, S., Deschênes, I., Disilvestre, D., Tian, Y., Halperin, V.L., and Tomaselli, G.F. (2008). Calmodulin regulation of Nav1.4 current: role of binding to the carboxyl terminus. J. Gen. Physiol. *131*, 197–209.

Biswas, S., DiSilvestre, D., Tian, Y., Halperin, V.L., and Tomaselli, G.F. (2009). Calcium-mediated dual-mode regulation of cardiac sodium channel gating. Circ. Res. *104*, 870–878.

Biswas, S., DiSilvestre, D.A., Dong, P., and Tomaselli, G.F. (2013). Mechanisms of a human skeletal myotonia produced by mutation in the C-terminus of NaV1.4: is Ca2+ regulation defective? PLoS ONE *8*, e81063.

Borst, J.G., and Sakmann, B. (1998). Facilitation of presynaptic calcium currents in the rat brainstem. J. Physiol. *513*, 149–155.

Bosmans, F., Martin-Eauclaire, M.F., and Swartz, K.J. (2008). Deconstructing voltage sensor function and pharmacology in sodium channels. Nature *456*, 202–208.

Brehm, P., and Eckert, R. (1978). Calcium entry leads to inactivation of calcium channel in *Paramecium*. Science *202*, 1203–1206.

Cannon, S.C. (1997). From mutation to myotonia in sodium channel disorders. Neuromuscul. Disord. *7*, 241–249.

Chagot, B., Potet, F., Balser, J.R., and Chazin, W.J. (2009). Solution NMR structure of the C-terminal EF-hand domain of human cardiac sodium channel NaV1.5. J. Biol. Chem. *284*, 6436–6445.

Chao, S.H., Suzuki, Y., Zysk, J.R., and Cheung, W.Y. (1984). Activation of calmodulin by various metal cations as a function of ionic radius. Mol. Pharmacol. *26*, 75–82.

Clausen, T. (2011). In isolated skeletal muscle, excitation may increase extracellular K+ 10-fold; how can contractility be maintained? Exp. Physiol. *96*, 356–368.

Crotti, L., Johnson, C.N., Graf, E., De Ferrari, G.M., Cuneo, B.F., Ovadia, M., Papagiannis, J., Feldkamp, M.D., Rathi, S.G., Kunic, J.D., et al. (2013). Calmodulin mutations associated with recurrent cardiac arrest in infants. Circulation *127*, 1009–1017.

de Leon, M., Wang, Y., Jones, L., Perez-Reyes, E., Wei, X., Soong, T.W., Snutch, T.P., and Yue, D.T. (1995). Essential Ca(2+)-binding motif for Ca(2+)-sensitive inactivation of L-type Ca2+ channels. Science *270*, 1502–1506.

DeMaria, C.D., Soong, T.W., Alseikhan, B.A., Alvania, R.S., and Yue, D.T. (2001). Calmodulin bifurcates the local Ca2+ signal that modulates P/Q-type Ca2+ channels. Nature *411*, 484–489.

Deschênes, I., Neyroud, N., DiSilvestre, D., Marbán, E., Yue, D.T., and Tomaselli, G.F. (2002). Isoform-specific modulation of voltage-gated Na(+) channels by calmodulin. Circ. Res. *90*, E49–E57.

Dunlap, K. (2007). Calcium channels are models of self-control. J. Gen. Physiol. *129*, 379–383.

Eckert, R., and Chad, J.E. (1984). Inactivation of Ca channels. Prog. Biophys. Mol. Biol. *44*, 215–267.

Erickson, M.G., Alseikhan, B.A., Peterson, B.Z., and Yue, D.T. (2001). Preassociation of calmodulin with voltage-gated Ca(2+) channels revealed by FRET in single living cells. Neuron *31*, 973–985.

Feldkamp, M.D., Yu, L., and Shea, M.A. (2011). Structural and energetic determinants of apo calmodulin binding to the IQ motif of the Na(V)1.2 voltage-dependent sodium channel. Structure *19*, 733–747.

Herzog, R.I., Liu, C., Waxman, S.G., and Cummins, T.R. (2003). Calmodulin binds to the C terminus of sodium channels Nav1.4 and Nav1.6 and differentially modulates their functional properties. J. Neurosci. *23*, 8261–8270.

Hille, B. (2001). Ionic Channels of Excitable Membranes, Third Edition (Sunderland, MA: Sinauer Associates).

Huang, H., Tan, B.Z., Shen, Y., Tao, J., Jiang, F., Sung, Y.Y., Ng, C.K., Raida, M., Köhr, G., Higuchi, M., et al. (2012). RNA editing of the IQ domain in Ca(v)1.3 channels modulates their Ca^{2+}-dependent inactivation. Neuron *73*, 304–316.

Imredy, J.P., and Yue, D.T. (1992). Submicroscopic Ca2+ diffusion mediates inhibitory coupling between individual Ca2+ channels. Neuron *9*, 197–207.

Imredy, J.P., and Yue, D.T. (1994). Mechanism of $Ca^{(2+)}$-sensitive inactivation of L-type Ca^{2+} channels. Neuron *12*, 1301–1318.

Jan, L.Y., and Jan, Y.N. (1989). Voltage-sensitive ion channels. Cell *56*, 13–25.

Kim, J., Ghosh, S., Liu, H., Tateyama, M., Kass, R.S., and Pitt, G.S. (2004a). Calmodulin mediates Ca2+ sensitivity of sodium channels. J. Biol. Chem. *279*, 45004–45012.

Kim, J., Ghosh, S., Nunziato, D.A., and Pitt, G.S. (2004b). Identification of the components controlling inactivation of voltage-gated Ca^{2+} channels. Neuron *41*, 745–754.

Kubota, T., Kinoshita, M., Sasaki, R., Aoike, F., Takahashi, M.P., Sakoda, S., and Hirose, K. (2009). New mutation of the Na channel in the severe form of potassium-aggravated myotonia. Muscle Nerve *39*, 666–673.

Lee, A., Wong, S.T., Gallagher, D., Li, B., Storm, D.R., Scheuer, T., and Catterall, W.A. (1999). Ca2+/calmodulin binds to and modulates P/Q-type calcium channels. Nature *399*, 155–159.

Liang, H., DeMaria, C.D., Erickson, M.G., Mori, M.X., Alseikhan, B.A., and Yue, D.T. (2003). Unified mechanisms of Ca^{2+} regulation across the Ca^{2+} channel family. Neuron *39*, 951–960.

Limpitikul, W.B., Dick, I.E., Joshi-Mukherjee, R., Overgaard, M.T., George, A.L., and Yue, D.T. (2014). Calmodulin mutations associated with long QT syndrome prevent inactivation of cardiac L-type Ca2+ currents and promote proarrhythmic behavior in ventricular myocytes. J. Mol. Cell. Cardiol *74*, 115–124.

Linse, S., and Forsén, S. (1995). Determinants that govern high-affinity calcium binding. Adv. Second Messenger Phosphoprotein Res. *30*, 89–151.

Mahajan, A., Sato, D., Shiferaw, Y., Baher, A., Xie, L.H., Peralta, R., Olcese, R., Garfinkel, A., Qu, Z., and Weiss, J.N. (2008). Modifying L-type calcium current kinetics: consequences for cardiac excitation and arrhythmia dynamics. Biophys. J. *94*, 411–423.

Miloushev, V.Z., Levine, J.A., Arbing, M.A., Hunt, J.F., Pitt, G.S., and Palmer, A.G., 3rd. (2009). Solution structure of the NaV1.2 C-terminal EF-hand domain. J. Biol. Chem. *284*, 6446–6454.

Mori, M., Konno, T., Ozawa, T., Murata, M., Imoto, K., and Nagayama, K. (2000). Novel interaction of the voltage-dependent sodium channel (VDSC) with calmodulin: does VDSC acquire calmodulin-mediated Ca2+-sensitivity? Biochemistry *39*, 1316–1323.

Mori, M.X., Erickson, M.G., and Yue, D.T. (2004). Functional stoichiometry and local enrichment of calmodulin interacting with Ca2+ channels. Science *304*, 432–435.

Peterson, B.Z., DeMaria, C.D., Adelman, J.P., and Yue, D.T. (1999). Calmodulin is the Ca^{2+} sensor for Ca2+ -dependent inactivation of L-type calcium channels. Neuron *22*, 549–558.

Peterson, B.Z., Lee, J.S., Mulle, J.G., Wang, Y., de Leon, M., and Yue, D.T. (2000). Critical determinants of Ca(2+)-dependent inactivation within an EF-hand motif of L-type Ca(2+) channels. Biophys. J. *78*, 1906–1920.

Pitt, G.S., Zühlke, R.D., Hudmon, A., Schulman, H., Reuter, H., and Tsien, R.W. (2001). Molecular basis of calmodulin tethering and Ca2+-dependent inactivation of L-type Ca2+ channels. J. Biol. Chem. *276*, 30794–30802.

Potet, F., Chagot, B., Anghelescu, M., Viswanathan, P.C., Stepanovic, S.Z., Kupershmidt, S., Chazin, W.J., and Balser, J.R. (2009). Functional Interactions between Distinct Sodium Channel Cytoplasmic Domains through the Action of Calmodulin. J. Biol. Chem. *284*, 8846–8854.

Preston, R.R., Kink, J.A., Hinrichsen, R.D., Saimi, Y., and Kung, C. (1991). Calmodulin mutants and Ca(2+)-dependent channels in Paramecium. Annu. Rev. Physiol. *53*, 309–319.

Prod'hom, B., Pietrobon, D., and Hess, P. (1987). Direct measurement of proton transfer rates to a group controlling the dihydropyridine-sensitive Ca2+ channel. Nature *329*, 243–246.

Sarhan, M.F., Tung, C.C., Van Petegem, F., and Ahern, C.A. (2012). Crystallographic basis for calcium regulation of sodium channels. Proc. Natl. Acad. Sci. USA *109*, 3558–3563.

Shah, V.N., Wingo, T.L., Weiss, K.L., Williams, C.K., Balser, J.R., and Chazin, W.J. (2006). Calcium-dependent regulation of the voltage-gated sodium channel hH1: intrinsic and extrinsic sensors use a common molecular switch. Proc. Natl. Acad. Sci. USA *103*, 3592–3597.

Sternweis, P.C., and Gilman, A.G. (1982). Aluminum: a requirement for activation of the regulatory component of adenylate cyclase by fluoride. Proc. Natl. Acad. Sci. USA *79*, 4888–4891.

Stühmer, W., Conti, F., Suzuki, H., Wang, X.D., Noda, M., Yahagi, N., Kubo, H., and Numa, S. (1989). Structural parts involved in activation and inactivation of the sodium channel. Nature *339*, 597–603.

Tadross, M.R., Tsien, R.W., and Yue, D.T. (2013). Ca2+ channel nanodomains boost local Ca2+ amplitude. Proc. Natl. Acad. Sci. USA *110*, 15794–15799.

Tan, H.L., Kupershmidt, S., Zhang, R., Stepanovic, S., Roden, D.M., Wilde, A.A., Anderson, M.E., and Balser, J.R. (2002). A calcium sensor in the sodium channel modulates cardiac excitability. Nature *415*, 442–447.

Trimmer, J.S., Cooperman, S.S., Agnew, W.S., and Mandel, G. (1990). Regulation of muscle sodium channel transcripts during development and in response to denervation. Dev. Biol. *142*, 360–367.

Van Petegem, F., Lobo, P.A., and Ahern, C.A. (2012). Seeing the forest through the trees: towards a unified view on physiological calcium regulation of voltage-gated sodium channels. Biophys. J. *103*, 2243–2251.

Wagner, S., and Maier, L.S. (2006). Modulation of cardiac Na(+) and Ca(2+) currents by CaM and CaMKII. J. Cardiovasc. Electrophysiol. *17* (*Suppl 1*), S26–S33.

Wang, C., Chung, B.C., Yan, H., Lee, S.Y., and Pitt, G.S. (2012). Crystal structure of the ternary complex of a NaV C-terminal domain, a fibroblast growth factor homologous factor, and calmodulin. Structure *20*, 1167–1176.

Wingo, T.L., Shah, V.N., Anderson, M.E., Lybrand, T.P., Chazin, W.J., and Balser, J.R. (2004). An EF-hand in the sodium channel couples intracellular calcium to cardiac excitability. Nat. Struct. Mol. Biol. *11*, 219–225.

Wu, F.F., Gordon, E., Hoffman, E.P., and Cannon, S.C. (2005). A C-terminal skeletal muscle sodium channel mutation associated with myotonia disrupts fast inactivation. J. Physiol. *565*, 371–380.

Yang, P.S., Alseikhan, B.A., Hiel, H., Grant, L., Mori, M.X., Yang, W., Fuchs, P.A., and Yue, D.T. (2006). Switching of Ca^{2+}-dependent inactivation of Ca(v)1.3 channels by calcium binding proteins of auditory hair cells. J. Neurosci. *26*, 10677–10689.

Zhou, J., Olcese, R., Qin, N., Noceti, F., Birnbaumer, L., and Stefani, E. (1997). Feedback inhibition of Ca2+ channels by Ca2+ depends on a short sequence of the C terminus that does not include the Ca2+ -binding function of a motif with similarity to Ca2+ -binding domains. Proc. Natl. Acad. Sci. USA *94*, 2301–2305.

Zimmer, T., and Surber, R. (2008). SCN5A channelopathies—an update on mutations and mechanisms. Prog. Biophys. Mol. Biol. *98*, 120–136.

Zühlke, R.D., and Reuter, H. (1998). Ca^{2+}-sensitive inactivation of L-type Ca^{2+} channels depends on multiple cytoplasmic amino acid sequences of the α_{1C} subunit. Proc. Natl. Acad. Sci. USA *95*, 3287–3294.

Zühlke, R.D., Pitt, G.S., Deisseroth, K., Tsien, R.W., and Reuter, H. (1999). Calmodulin supports both inactivation and facilitation of L-type calcium channels. Nature *399*, 159–162.

Zühlke, R.D., Pitt, G.S., Tsien, R.W., and Reuter, H. (2000). Ca2+-sensitive inactivation and facilitation of L-type Ca2+ channels both depend on specific amino acid residues in a consensus calmodulin-binding motif in the(alpha)1C subunit. J. Biol. Chem. *275*, 21121–21129.

EXTENDED EXPERIMENTAL PROCEDURES

Construction of Na_V and Ca_V Channel Mutants and Chimeras

To facilitate mutagenesis of $Na_V1.4$ carboxy terminus, we first PCR amplified and subcloned an ~900 bp segment containing the CI region (bounded by KpnI and XbaI restriction sites) into zero blunt TOPO II (Invitrogen) vector, yielding a convenient TOPO-$Na_V1.4$CT construct. Quikchange (Agilent) was then used to introduce channel EF-hand mutations (D[1621]A & D[1623]A in Figure 5A; and 4 × mutations in Figure S6B), alanine substitutions of isoleucine and glutamine residues of IQ domain (Figure 5G), and channelopathic mutations (Q[1626]E in Figure 6C; and F[1698]I in Figure 6D) into the TOPO-$Na_V1.4$CT construct. These mutant segments were then transferred to $Na_V1.4$ pcDNA3 construct following restriction digest and ligation utilizing KpnI/XbaI sites.

To generate the $Na_V1.4$-$Na_V1.5$CT chimeric channel (Figure 5F), we first introduced a silent XhoI site immediately downstream of the channel domain IV S6 segment (5212-ctGgag-5217 to 5212-ctCgag-5217) using Quikchange (Agilent) on TOPO-$Na_V1.4$CT construct followed by ligation into the full length $Na_V1.4$ clone. Subsequently, the entire $Na_V1.5$ carboxy-terminus starting at 1772-LENFSV-1778 was PCR amplified and cloned into $Na_V1.4$ utilizing restriction sites XhoI and XbaI.

A similar strategy was followed for mutagenesis of the III-IV loop mutation (Y[1311]A, Figure 5E). An ~3300 bp segment bounded by unique restriction sites BsiWI and KpnI including the III-IV loop was subcloned into zero blunt Topo II (Invitrogen) vector following PCR amplification. The Y[1311]A mutation was then introduced into this segment using Quikchange (Agilent), and subsequently transferred to the full length channel.

To construct $Na_V1.5$-$Na_V1.4$CT chimera (Figure 7A), we introduced a silent NruI site into $Na_V1.5$ channel by mutagenesis of location 5329–gtggccacg–5337 into 5329–gtCgcGacg–5337. Subsequently, the entire $Na_V1.4$CT was PCR amplified starting at residue location 1596-VAT-1599 and ligated into full length $Na_V1.5$ exploiting the NruI/XbaI sites.

To construct the $Ca_V1.3$-$Na_V1.4$CT chimera (Figure 7B), we first truncated the $Ca_V1.3$ channel immediately upstream of the EF hand region (terminating with residues 1471–ILGPHHLD–1479) and concurrently introduced a silent XbaI site at residue HLD by mutating base pairs, 4426–caccacttggac–4437 into 4426–caccaTCTAgac–4437 using PCR amplification and ligation utilizing BglII/XbaI restriction sites. Subsequently, the $Na_V1.4$CT was PCR amplified using primers: (fwd) 5′-caccaTCTAgacatgttctatgagacctgggag-3′ and (rev) 5′-gatagagtttaaacttagacaagagactctttgacccc-3′ and ligated into the truncated $Ca_V1.3$ construct using XbaI/PmeI restriction sites. This maneuver created the $Ca_V1.3$-$Na_V1.4$CT chimera with the protein sequence 1471-ILGPHHLDMFYEIW-1485 at the amino-terminal segment of the EF hand region (Figure 1A).

All segments subjected to PCR amplification and Quikchange mutagenesis were verified by sequencing.

Transfection of HEK293 Cells

For whole-cell patch clamp experiments, HEK293 cells were cultured on 10-cm plates, and channels transiently transfected by calcium phosphate method (Peterson et al., 1999). For experiments involving static Ca^{2+} (Figures 1F–1H and S1), we cotransfected 6 μg of rat $Na_V1.4$ or 6 μg of human $Na_V1.5$ with 8 μg of eYFP. For Ca^{2+} uncaging experiments (Figures 2, 3, 5, 6C, and 6D), we applied 6-8 μg of cDNA encoding the desired Na channel, 6 μg of eCFP, and 8 μg of rat CaM_{WT}. For experiments involving mutant CaM, we substituted 8 μg of CaM_{12}, CaM_{34}, or CaM_{1234} instead of CaM_{WT}. For experiments that involved both $Ca_V2.1$ and Na channels at the whole-cell level (Figure 3), 6 μg rat $Na_V1.4$ or $Na_V1.5$, 8 μg of α_1 subunit of $Ca_V2.1$ EFb $43^+/44^-/47^+$ isoform (Chaudhuri et al., 2004), 8 μg of rat brain β_{2a} (*M80545*) auxiliary subunit, 5 μg of $\alpha_2\delta$ (*NM012919.2*), and 8 μg of rat CaM_{WT} or 8 μg of CaM_{1234} (Figures S6D and S6E) were cotransfected. For like coexpression experiments at the single-channel level (Figure 4), 1-2 μg rat $Na_V1.4$, 8-10 μg of α_1 subunit of $Ca_V2.1$ EFb $43^+/44^-/47^+$ isoform (Chaudhuri et al., 2004), 8 μg of rat brain β_{2a} (*M80545*) auxiliary subunit, 5 μg of $\alpha_2\delta$ (*NM012919.2*), and 8 μg of rat CaM_{WT} were cotransfected. For experiments probing Ca^{2+} channel CDI (Figures 1C, 7C, and 7D), we cotransfected 8 μg of $Ca_V1.3$ or $Ca_V1.3$-$Na_V1.4$CT, 8 μg of rat brain β_{2a} auxiliary subunit, 5 μg of $\alpha_2\delta$, and 8 μg of rat CaM_{WT} or 8 μg of mutant CaM_{1234} All of the above cDNA constructs were included within mammalian expression plasmids driven by a cytomegalovirus promoter. To boost expression, cDNA for simian virus 40 T antigen (1-2 μg) was cotransfected. Currents were probed ~1-3 days following transfection.

Detailed Recipes for Pipet and Bath Solutions

For recordings of wild-type $Ca_V1.3$ (Figure 1C) and $Ca_V1.3$ III-IV_{17A} mutant (Figure S7C), we used an internal solution, "0 [Ca^{2+}]," which contained (in mM): $CsMeSO_3$, 114; CsCl, 5; $MgCl_2$, 1; MgATP, 4; HEPES (pH 7.4), 10; and BAPTA, 10; at 290 mOsm adjusted with glucose. The bath solution contained (in mM): TEA-$MeSO_3$, 102; HEPES (pH 7.4), 10; $CaCl_2$ or $BaCl_2$, 40; at 300 mOsm adjusted by TEA-$MeSO_3$. For recordings of $Ca_V1.3$-$Na_V1.4$CT chimeric channel, we used the same bath solution and a modified internal solution containing (in mM): $CsMeSO_3$, 124; CsCl, 5; $MgCl_2$, 1; MgATP, 4; HEPES (pH 7.4), 10; and EGTA, 0.5; at 290 mOsm adjusted with glucose.

For experiments probing Na_V steady-state inactivation under static Ca^{2+} (Figures 1F–1H), we used either "0 [Ca^{2+}]" solution described above, or a "10 [Ca^{2+}]" solution containing (in mM): $CsMeSO_3$, 109; CsCl, 5; $MgCl_2$, 1; MgATP, 4; HEPES (pH 7.4), 10; HEDTA, 10; and $CaCl_2$, 5, at 290 mOsm adjusted with glucose. The bath solution contained (in mM): TEA-$MeSO_3$, 45; HEPES (pH 7.4), 10; NaCl, 100; at 300 mOsm adjusted with TEA-$MeSO_3$. The electrophysiological measurements were obtained only after ~10 min of pipet dialysis to permit stabilization of Na channel properties.

For all Ca^{2+}-uncaging experiments, internal solution contained (in mM): $CsMeSO_3$, 120; CsCl, 5; HEPES (pH 7.4 with CsOH), 10; Fluo-4FF pentapotassium salt (Invitrogen), 0.01; Alexa 568 succinimidyl ester (Invitrogen), 0.0025; Citrate, 1; DM-Nitrophen EDTA (DMN) and $CaCl_2$ were adjusted to obtain desired Ca^{2+} flash. Typically, for flashes in range 0.5 – 2 μM, DMN, 1 mM; and $CaCl_2$, 0.7 mM. For the 2 – 8 μM range, DMN, 2 mM; and $CaCl_2$, 1.4 mM. For larger Ca^{2+} steps, DMN, 4 mM; and $CaCl_2$, 3.2 mM. Since DMN can bind Mg^{2+}, all experiments were conducted with 0 mM Mg^{2+} internally. For recombinant Na channel experiments, the bath solution contained (in mM): TEA-$MeSO_3$, 45; HEPES (pH 7.4), 10; NaCl, 100; at 300 mOsm, adjusted with TEA-$MeSO_3$. For Ca^{2+} uncaging experiments in guinea pig ventricular myocytes, we used a modified bath solution containing (in mM): NaCl, 2; Choline-Cl, 125; $CaCl_2$, 5; KCl, 4; HEPES, 10; glucose, 10; adjusted to pH 7.4 with NaOH and 300 mOsm with Choline-Cl. For Ca^{2+}-uncaging experiments in GLT cells, the bath solution contained (in mM): NaCl, 100; HEPES (pH 7.4), 10; Choline-Cl, 35; $MgCl_2$, 1; KCl, 4; at 290 mOsm adjusted with Choline-Cl.

For experiments coexpressing both Na_V and Ca_V channels (Figure 3), the bath solution contained (in mM): NaCl, 130; $CaCl_2$, 15; $MgCl_2$, 1; KCl, 4; NaH_2PO_4, 0.33; HEPES, 10; with pH 7.4 adjusted with NaOH and at 290 mOsm adjusted with NaCl. For corresponding control experiments that used Ba^{2+} as charge carrier through Ca^{2+} channels, we substituted 15 mM $BaCl_2$ in place of $CaCl_2$. The pipet solution, "0.5 EGTA" contained (in mM): $CsMeSO_3$, 124; CsCl, 5; $MgCl_2$, 1; MgATP, 4; HEPES (pH 7.4), 10; and EGTA, 0.5; at 290 mOsm adjusted with glucose. For high internal buffering (Figures 3H–3K), we used "0 [Ca^{2+}]" solution described above.

For multi-channel on-cell recordings of Na channels cotransfected with Ca^{2+} channels (Figure 4), the bath solution contained (in mM): K-glutamate, 132; KCl, 5; NaCl, 5; $MgCl_2$, 3; EGTA, 2; Glucose, 6; and HEPES, 10 (pH adjusted to 7.4). The pipet solution contained (in mM): TeA-$MeSO_3$, 30; NaCl, 100; $CaCl_2$, 10; HEPES, 10 (pH 7.4).

Ca^{2+} Measurements

Ca^{2+} measurements were determined from ratio of Fluo4FF/Alexa fluorescence intensities (R), according to the relation $[Ca^{2+}] = K_d \cdot (R - R_{min}) / (R_{max} - R)$. All three parameters K_d, R_{min}, R_{max} were experimentally determined in HEK293 cells dialyzed with reference Ca^{2+} solutions (Tadross et al., 2013) and were assumed to be same for ventricular myocytes and GLT cells. Briefly, R_{min} was determined with internal solution containing 40 mM EGTA, and R_{max} using 4 mM Ca^{2+}/1 mM EGTA (~3 mM free Ca^{2+}) solution. An $R_{20\ \mu M}$ measurement was obtained with internal solution containing $[Ca^{2+}]$ = 20 μM (buffered using NTA). K_d was experimentally determined by solving the equation above. Calibration measurements were repeated at 1 or 4 mM DMN to account for minor differences in R_{max}.

Construction of Phylogenetic Tree

For Figure 7B, protein sequences of all human Ca_V1, Ca_V2, Ca_V3 and Na_V1 channels were obtained from GenBank (Benson et al., 2005). For Figure 7C, protein sequences were acquired from GenBank (Benson et al., 2005), UniProt (UniProt Consortium, 2013), JGI (Grigoriev et al., 2012), or ParameciumDB (Arnaiz and Sperling, 2011) databases. Multiple sequence alignments were made using MUSCLE algorithm (Edgar, 2004) and phylogenetic trees were constructed using MEGA5.2 software (Tamura et al., 2011).

Isolation of Guinea Pig Ventricular Myocytes

Ventricular myocytes were isolated from adult guinea pigs in accordance with guidelines established by Johns Hopkins University Animal Care and Use Committee as described in previous publication (Alseikhan et al., 2002). Briefly, hearts were excised and ventricular myocytes were isolated by enzymatic digestion using a Langendorff perfusion apparatus. Whole-cell Na currents were interrogated using patch clamp ~2 hr after isolation.

GLT Myoblast Culture

Homozygous mouse dysgenic (mdg/mdg) GLT cell lines were originally generated by stable transfection of mdg myoblasts with plasmid-encoding large-T antigen (Powell et al., 1996). The myoblasts were expanded in growth media based of F-10 Ham's media containing 20% FBS; HEPES, 25 mM; L-glutamine, 4 mM; Penicillin-Streptomycin, 100 U/ml; and βFGF, 1 ng/ml. After reaching more than 90% confluence (~3 days), the growth media was exchanged for a DMEM based differentiation media that contains 2% horse serum, Penicillin-streptomycin, 100 U/ml; and L-glutamine, 4 mM. Following differentiation (~3 days), the cells were split onto glass coverslips and patch clamp experiments were conducted the following day.

SUPPLEMENTAL REFERENCES

Aiba, T., Hesketh, G.G., Liu, T., Carlisle, R., Villa-Abrille, M.C., O'Rourke, B., Akar, F.G., and Tomaselli, G.F. (2010). Na^+ channel regulation by Ca^{2+}/calmodulin and Ca^{2+}/calmodulin-dependent protein kinase II in guinea-pig ventricular myocytes. Cardiovasc. Res. *85*, 454–463.

Arnaiz, O., and Sperling, L. (2011). ParameciumDB in 2011: new tools and new data for functional and comparative genomics of the model ciliate Paramecium tetraurelia. Nucleic Acids Res. *39* (Database issue), D632–D636.

Ashpole, N.M., Herren, A.W., Ginsburg, K.S., Brogan, J.D., Johnson, D.E., Cummins, T.R., Bers, D.M., and Hudmon, A. (2012). Ca^{2+}/calmodulin-dependent protein kinase II (CaMKII) regulates cardiac sodium channel $Na_V1.5$ gating by multiple phosphorylation sites. J. Biol. Chem. *287*, 19856–19869.

Benson, D.A., Karsch-Mizrachi, I., Lipman, D.J., Ostell, J., and Wheeler, D.L. (2005). GenBank. Nucleic Acids Res. *33* (Database issue), D34–D38.

Chaudhuri, D., Chang, S.Y., DeMaria, C.D., Alvania, R.S., Soong, T.W., and Yue, D.T. (2004). Alternative splicing as a molecular switch for Ca^{2+}/calmodulin-dependent facilitation of P/Q-type Ca^{2+} channels. J. Neurosci. *24*, 6334–6342.

Edgar, R.C. (2004). MUSCLE: multiple sequence alignment with high accuracy and high throughput. Nucleic Acids Res. *32*, 1792–1797.

Erickson, M.G., Liang, H., Mori, M.X., and Yue, D.T. (2003). FRET two-hybrid mapping reveals function and location of L-type Ca^{2+} channel CaM preassociation. Neuron *39*, 97–107.

Grigoriev, I.V., Nordberg, H., Shabalov, I., Aerts, A., Cantor, M., Goodstein, D., Kuo, A., Minovitsky, S., Nikitin, R., Ohm, R.A., et al. (2012). The genome portal of the Department of Energy Joint Genome Institute. Nucleic Acids Res. *40* (Database issue), D26–D32.

Powell, J.A., Petherbridge, L., and Flucher, B.E. (1996). Formation of triads without the dihydropyridine receptor alpha subunits in cell lines from dysgenic skeletal muscle. J. Cell Biol. *134*, 375–387.

Tamura, K., Peterson, D., Peterson, N., Stecher, G., Nei, M., and Kumar, S. (2011). MEGA5: molecular evolutionary genetics analysis using maximum likelihood, evolutionary distance, and maximum parsimony methods. Mol. Biol. Evol. *28*, 2731–2739.

UniProt Consortium (2013). Update on activities at the Universal Protein Resource (UniProt) in 2013. Nucleic Acids Res. *41* (Database issue), D43–D47.

West, J.W., Patton, D.E., Scheuer, T., Wang, Y., Goldin, A.L., and Catterall, W.A. (1992). A cluster of hydrophobic amino acid residues required for fast $Na(^{+})$-channel inactivation. Proc. Natl. Acad. Sci. USA *89*, 10910–10914.

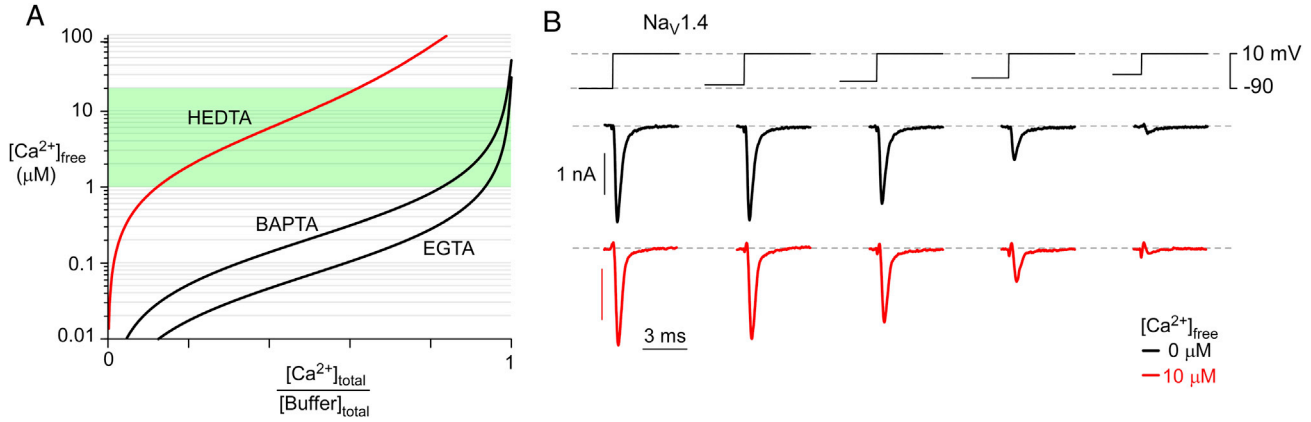

Figure S1. Static Ca^{2+} Buffering to Probe Na Channel Regulation, Related to Figure 1

(A) Theoretical simulation of Ca^{2+} buffering using EGTA, BAPTA, and HEDTA as buffers. The concentration of free $[Ca^{2+}]$ is plotted against the ratio of total Ca^{2+} to total buffer ($[Ca^{2+}]_{total}$ / $[Buffer]_{total}$), with $[Buffer]_{total}$ = 10 mM. In general, a buffer is most effective at maintaining free Ca^{2+} concentrations near its Ca^{2+} dissociation constant. Thus, EGTA and BAPTA (black lines) having K_d = 67 nM and 192 nM respectively, are effective at buffering Ca^{2+} in the 30–600 nM concentration range, but become rather ineffective at higher Ca^{2+} concentrations. For instance, to attain $[Ca^{2+}]_{free}$ ~10 μM with these buffers, $[Ca^{2+}]_{total}$ must approximately equal $[Buffer]_{total}$. In this regime, most buffer molecules are already bound to a Ca^{2+} ion and, therefore, any excess contaminant ions will be unbuffered. Thus, small pipeting errors and stray Ca^{2+} ions from the experimental setting could amount to large fluctuations of $[Ca^{2+}]_{free}$ in the pipet. By contrast, HEDTA (red line) with K_d = 4 μM is an ideal buffer to clamp $[Ca^{2+}]_{free}$ in the 1–20 μM range. This simulation accounts for the precise experimental conditions used in this study (10 mM HEDTA, 4 mM ATP, 5 mM Mg^{2+}). So with HEDTA as buffer, $[Ca^{2+}]_{free}$ can be effectively maintained near ~10 μM.

(B) Exemplar $Na_V1.4$ currents evoked using steady-state inactivation protocol (Figure 1E) with 0 μM (black) or 10 μM internal $[Ca^{2+}]$ (red). The fractional current remaining appears similar in both conditions. Population averages shown in Figure 1H further confirm that the voltage dependence of steady inactivation is unaltered by Ca^{2+}.

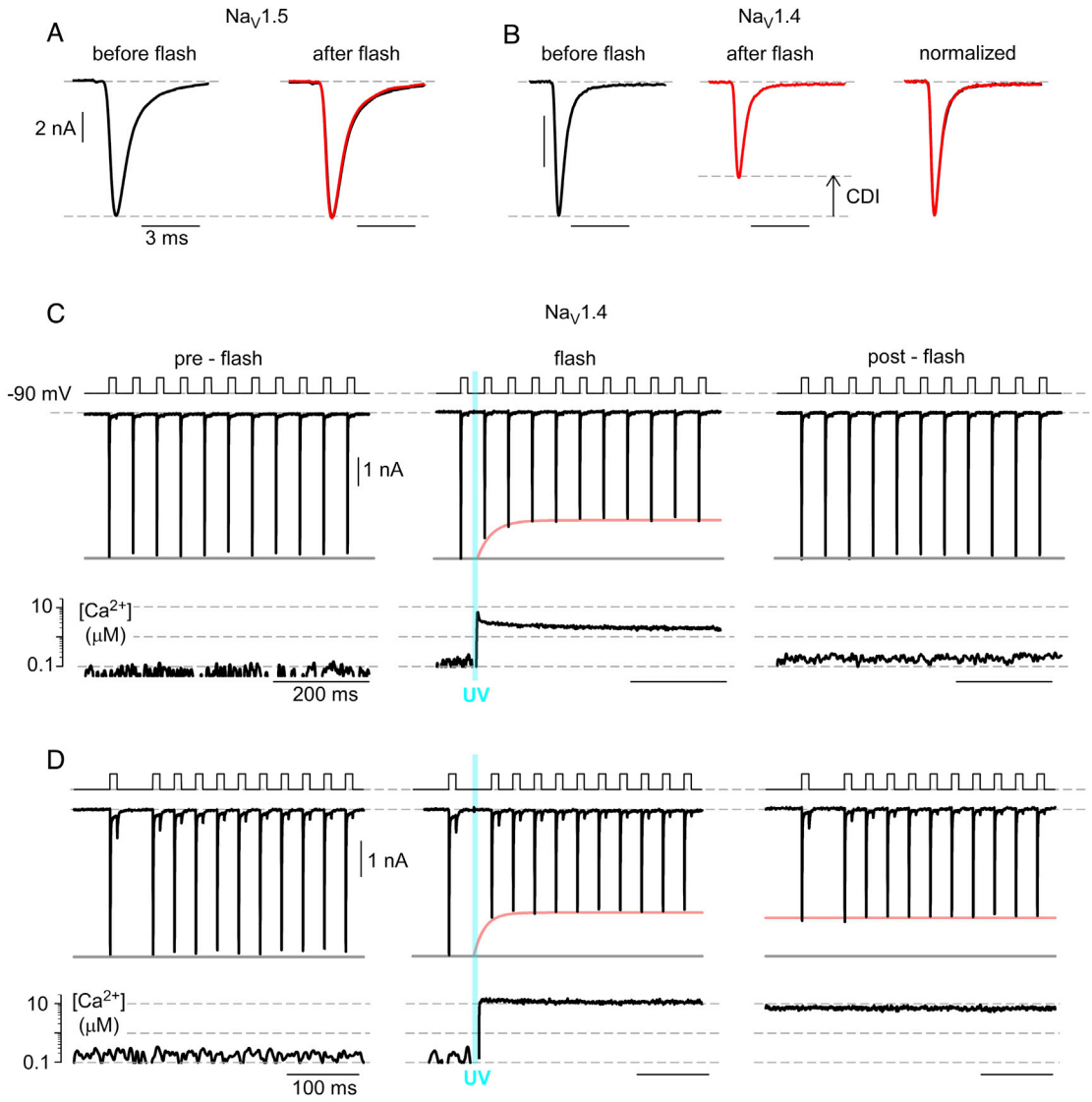

Figure S2. Extended Data Showing Effects of Ca^{2+} Uncaging on Na Channels, Related to Figure 2

(A) To probe whether Ca^{2+} alters the kinetics of Na channel activation and inactivation, we scrutinized the Na current waveform obtained from protocols analogous to those in main text Figures 2A and 2B. Left, Na current obtained prior to Ca^{2+} uncaging. Right, current evoked 900 ms after the onset of Ca^{2+} elevation (red trace) overlaid on the waveform before uncaging (black trace underneath, copied from left subpanel). Remarkably, the traces overlay suggesting that Ca^{2+} has no effect on the $Na_V1.5$ current waveform morphology. Here, the current traces are plotted on an expanded time-base so as to reveal both kinetics of activation and inactivation.

(B) Left, $Na_V1.4$ current before Ca^{2+} uncaging (Pulse #1 Figure 2B). Middle, Na current amplitude after Ca^{2+} uncaging (pulse #11 obtain after ~450 ms after Ca^{2+} uncaging) is reduced by ~30%. Right, normalized current after uncaging shows unperturbed activation and inactivation kinetics in presence of Ca^{2+} (red trace after uncaging plotted on top of black trace before uncaging).

(C) Exemplar $Na_V1.4$ currents show CDI and recovery from CDI following return of Ca^{2+} to resting levels. Format as in main text Figure 2B. Left, Na current evoked by pulse train prior to Ca^{2+} uncaging. Middle, onset of CDI as evident from decrement of Na current following Ca^{2+} step to ~2 μM. Right, once intracellular Ca^{2+} returned to basal levels (~150 nM), the Na current amplitude also recovered.

(D) In a different cell, when the cytosolic Ca^{2+} remained high after uncaging to ~10 μM Ca^{2+}, the Na current amplitude also remained at the inactivated level, confirming the exquisite Ca^{2+} dependence of this novel type of modulation.

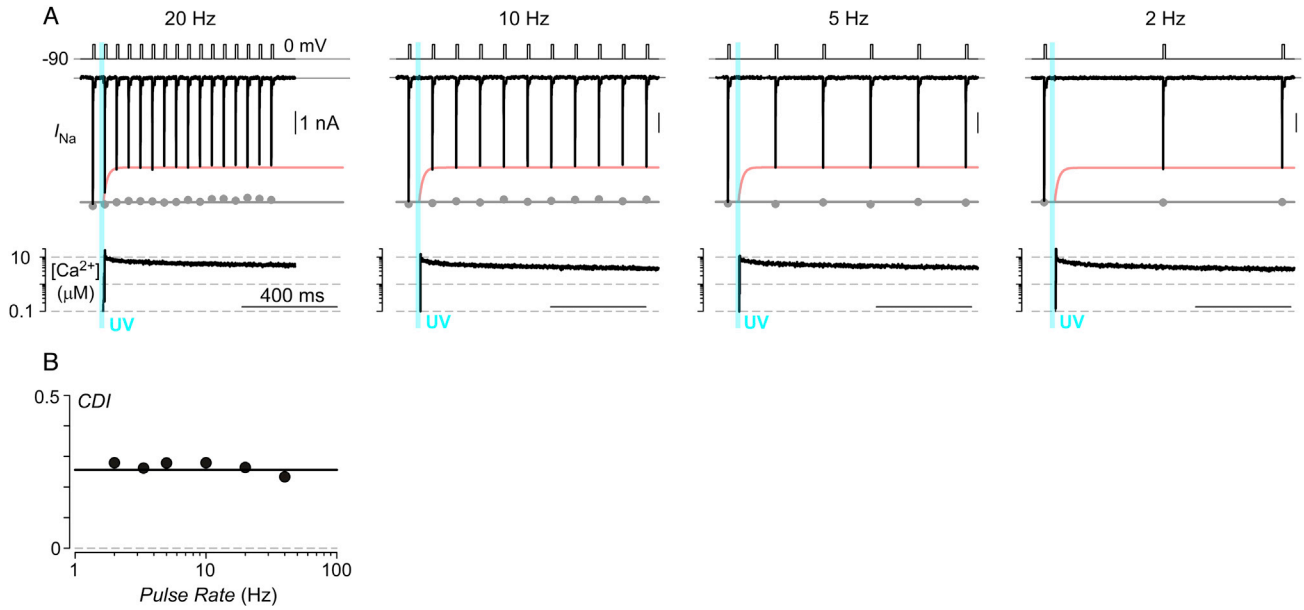

Figure S3. Effects of Pulse Rate on $Na_V1.4$ Channel CDI, Related to Figure 2

(A) Since Na channels undergo fast inactivation within the first few milliseconds following depolarization, the time course and magnitude of the slower Ca^{2+}-dependent regulation of Na channels was deduced from the "envelope" of peak Na currents pulsed at regular intervals after Ca^{2+} uncaging. To ensure that $Na_V1.4$ Ca^{2+} regulation is independent of this pulse rate, CDI was characterized for Na currents evoked at multiple pulse rates in a single cell. Gray dots and fit correspond to peak currents prior to Ca^{2+} uncaging. Following Ca^{2+} uncaging (cyan line), current amplitudes declined rapidly, revealing CDI in response to ~5 μM Ca^{2+} steps. Format as in Figure 2B. Red envelope curves are identical for various pulse rates, confirming that the onset of CDI is independent of pulse rate.

(B) Summary relationship further confirms that CDI magnitude (obtained from records in panel A) is independent of the pulse rate used to evoke $Na_V1.4$ current.

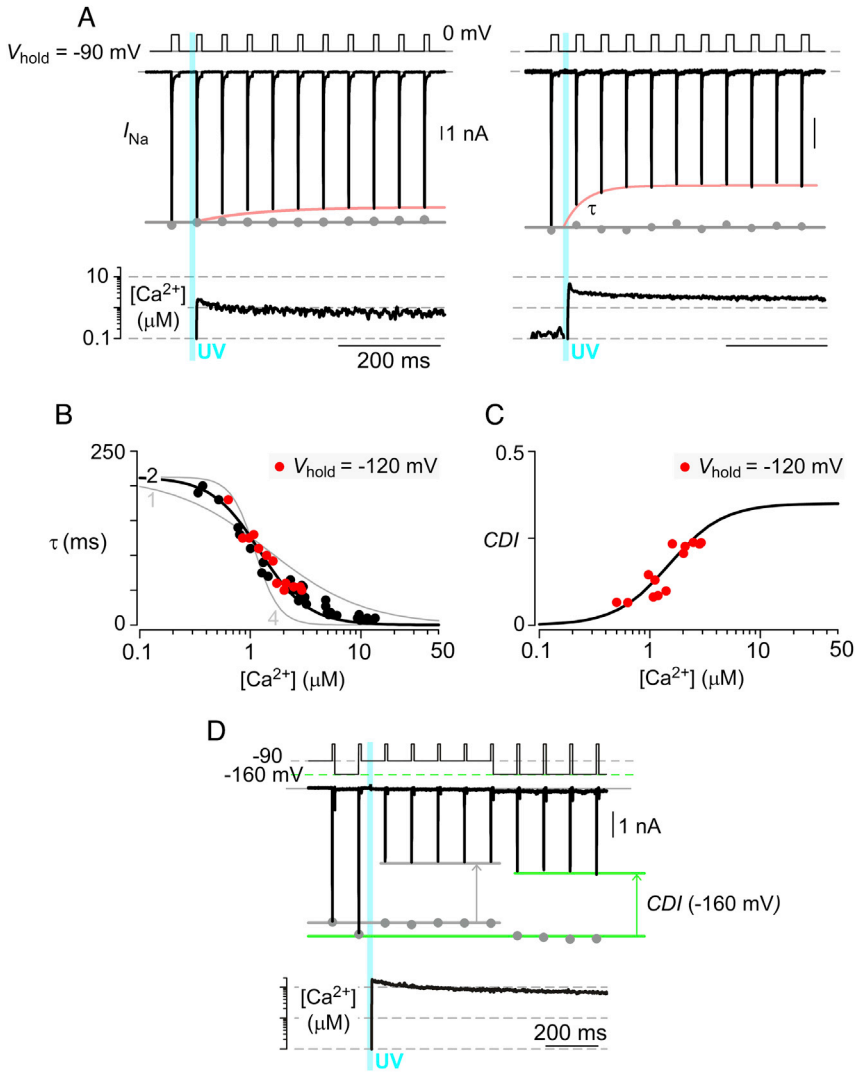

Figure S4. Kinetics of $Na_V1.4$ CDI, Ca^{2+} Dependence, and Voltage Independence, Related to Figure 2

(A) CDI elicited by Ca^{2+} steps of different amplitudes. The time constant (τ) for the onset of CDI was estimated by single exponential fits to peak current amplitudes following Ca^{2+} uncaging ("red envelope"). Left, CDI onset is slower in response to a smaller Ca^{2+} step. Right, CDI onset is much faster with a larger Ca^{2+} step. Format as in main text Figure 2B.

(B) The time constant of CDI onset (τ) plotted versus the magnitude of Ca^{2+} step with holding potential (V_{hold}) near −90 mV (n = 21 cells). This relation is well approximated (black fit) by system where channels transition from a normal mode of gating to a reduced-probability mode of gating via a rate constant given by $k_{on} \times [Ca^{2+}]^n$, with return rate constant k_{off}. Specifically, $k_{on} = 3.2 \times 10^{12}\ M^{-2}s^{-1}$, $k_{off} = 4.7\ s^{-1}$, and Hill coefficient n = 2. Indeed, it is reassuring that $(k_{off} / k_{on})^{1/2}$ ~1.5 μM is consistent with the measured K_d of steady-state *CDI*–$[Ca^{2+}]$ relations (Figure 2B). Gray fit, predicted relations for hill coefficient n = 1 or n = 4 diverge from the experimental data. Overall, these results conform well with the dominance of a single lobe (N-lobe) of CaM in triggering CDI (Figures 5C and 5D). Red symbols, τ – $[Ca^{2+}]$ relation obtained with holding potential set to −120 mV also overlay same relation, again consistent with CDI being a largely Ca^{2+}-dependent process.

(C) Steady-state relation for CDI versus Ca^{2+} concentration, obtained with V_{hold} = −120 mV, overlays standard black relation reproduced from Figure 2B. Thus, the steady-state extent of $Na_V1.4$ CDI also appears independent of the holding potential.

(D) CDI is not reversed by setting holding potential to −160 mV. After evoking CDI at −90 mV (horizontal gray lines), changing to −160 mV does not change the extent of inhibition (horizontal green lines). These results agree with a scaling down of steady-state inactivation (Figure 2D).

Overall, $Na_V1.4$ channel CDI appears primarily a function of Ca^{2+} binding and unbinding to a resident calmodulin that indwells the channel. CDI is not a strong function of voltage and/or pattern of voltage activation.

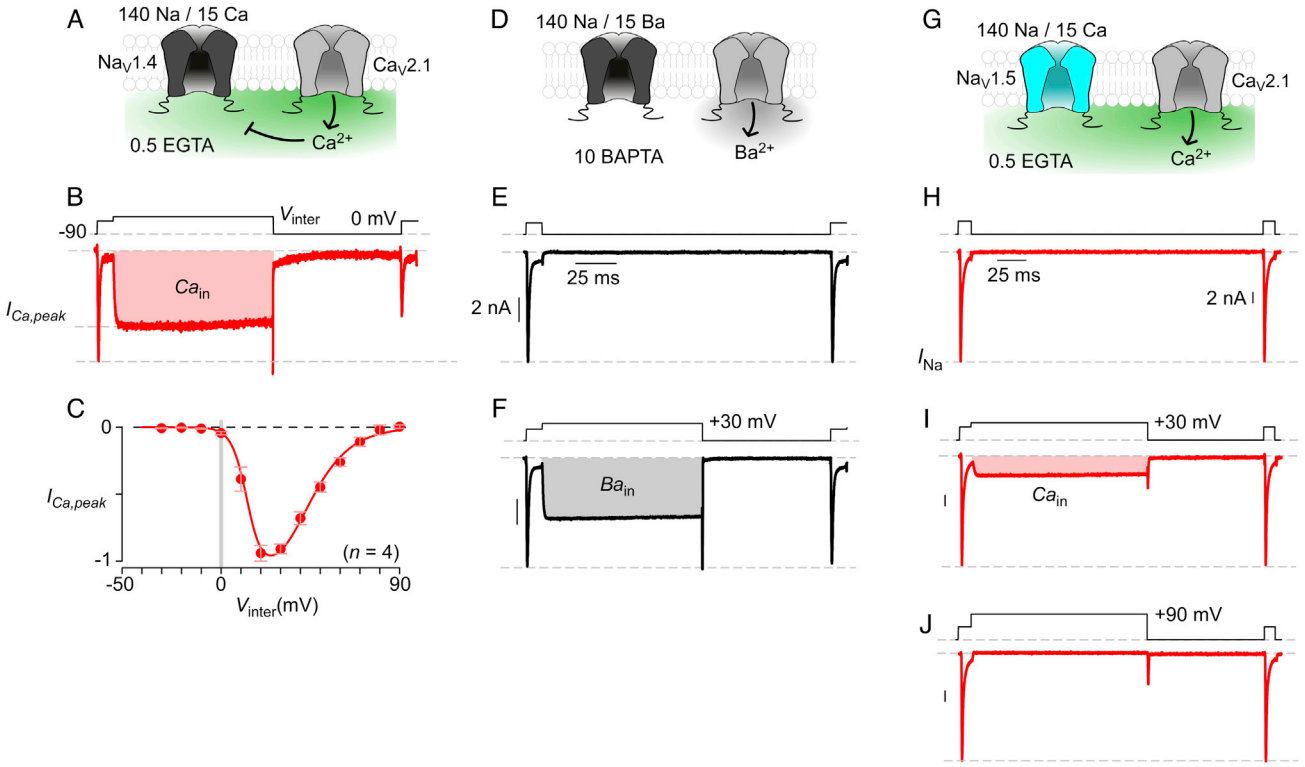

Figure S5. Na Channel Ca^{2+} Regulation by Ca^{2+} Spillover from Ca^{2+} Channels, Related to Figure 3

(A) In native systems, voltage-gated Ca^{2+} channels constitute a prominent source for Ca^{2+} influx. Could Ca^{2+} entry through such physiological sources trigger Na channel Ca^{2+} regulation? Accordingly, we coexpress $Na_V1.4$ channels with $Ca_V2.1$ channels, chosen deliberately for their higher threshold for voltage activation that enables selective measurement of Na currents at lower voltages. The schematic thus illustrates the experimental paradigm used in Figure 3, where Ca^{2+} spillover from Ca^{2+} channels was used to drive $Na_V1.4$ CDI.

(B) Top, stimulus protocol used to probe $Na_V1.4$ CDI. An initial depolarizing pulse to 0 mV was used to evoke Na current. Immediately following, a family of voltage pulses (V_{inter}) was applied to activate Ca^{2+} currents. Since Na channels undergo fast inactivation, the peak current measured during the intervening pulse (V_{inter}) represents the peak Ca^{2+} current at a given voltage ($I_{Ca,peak}$).

(C) Here, peak Ca^{2+} current thus measured during the intervening pulse is plotted against corresponding V_{inter} to reveal the current–voltage relationship for $Ca_V2.1$. Indeed at 0 mV, Ca^{2+} channels are minimally activated (<5%), thus enabling activation of Na current alone at this potential. Each symbol, mean ± SEM from 4 cells.

(D–F) Restricting Ca^{2+} elevations to the Ca^{2+} channel nanodomain by utilizing fast Ca^{2+} buffering eliminates CDI of $Na_V1.4$ driven by Ca^{2+} influx through $Ca_V2.1$ (Figures 3H–3K). Here, we furnish control experiments that utilize Ba^{2+} as permeant ion through Ca^{2+} channel. Format as in Figures 3H–3J. Indeed, Na current amplitude is unperturbed by Ba^{2+} influx through Ca^{2+} channel. Similar data were used to calculate black symbols in Figure 3K.

(G–J) A useful aspect of these whole-cell experiments utilizing coexpression of Na and Ca^{2+} channels is that Na channel CDI can be evoked independent of UV uncaging of Ca^{2+} complexed with DM nitrophen, allowing us to control for potential artifacts that may result from release of photolytic products. To complete the control experiments that may be performed in this vein, we coexpress $Na_V1.5$ and $Ca_V2.1$ channels and utilize a dual-pulse protocol to probe for Ca^{2+} regulation. Indeed even in this mode, we observe no indication of CDI of $Na_V1.5$, consistent with results obtained with Ca^{2+} uncaging experiments. Format identical to that in Figures 3A–3D. Importantly, 0.5 mM EGTA is the internal Ca^{2+} buffer, so as to permit robust Ca^{2+} spillover from Ca^{2+} channels.

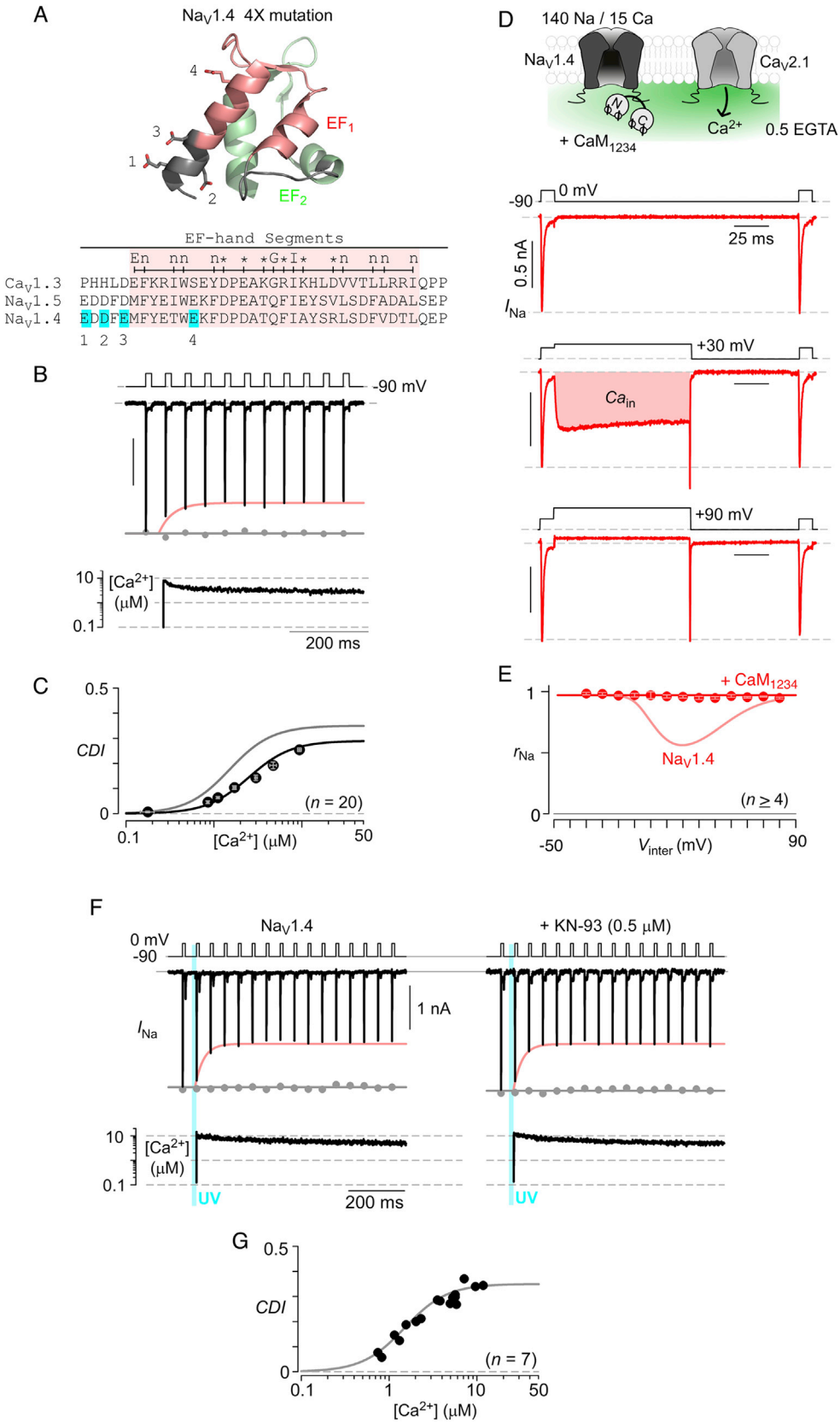

(legend on next page)

Figure S6. $Na_V1.4$ CDI Relies on CaM but Is Spared by Channel EF Mutations and CaMKII Inhibition, Related to Figure 5

(A–C) Extended data show that EF-hand region is not the primary Ca^{2+} sensing element for Na channel regulation.

(A) Based on homology modeling, four oxygen-bearing residues of the $Na_V1.5$ EF hand region were historically proposed to support direct binding of Ca^{2+} to Na channel that presumably triggered channel modulation (Biswas et al., 2009; Wingo et al., 2004). Top, atomic structures (Miloushev et al., 2009; Wang et al., 2012) of $Na_V1.5$ EF hand segment showing these four residues (as labeled) cannot coordinate Ca^{2+}. Bottom, sequence alignment depicting location of these four residues of Na channels argued to bind Ca^{2+}. Nonetheless, we undertook alanine substitutions of corresponding residues on $Na_V1.4$ (E[1621]A, D[1623]A, E[1625]A, E[1632]A – termed 4× mutations) to test for Ca^{2+} regulatory effects.

(B) Ca^{2+} uncaging experiments, however, show that $Na_V1.4$ channels with the 4× mutation can undergo robust CDI, much like the alternative EF hand mutations described in Figure 5A (D[1621]A and D[1623]A). Here, exemplar Na current shows CDI in response to ~3 μM Ca^{2+} step. Format as in main text Figure 2B.

(C) Population average shows average *CDI* as a function of [Ca^{2+}] (black symbols and trace). Gray trace, fit for wild-type channels from Figure 2B. Indeed, these outcomes sharply contrast with the complete knockout of CDI observed using CaM_{1234} overexpression with wild-type $Na_V1.4$ channels (Figure 5B). The minor reduction in maximal *CDI*, and the slightly weakened Ca^{2+} affinity may hint at a potential role for this region as a CDI transduction element. Indeed, in Ca^{2+} channels, the EF-hand region is thought to bind to the C-lobe of Ca^{2+}/CaM and the IQ domain to form a tripartite complex that serves as an effector configuration for CDI of these channels (Ben Johny et al., 2013). A variation on this theme may furnish a parsimonious mechanistic basis for Na channel Ca^{2+} regulation. Each symbol, mean ± SEM from 9-10 uncaging events compiled from 20 cells.

(D–E) Na channel regulation by Ca^{2+} spillover from nearby Ca^{2+} channels is mediated by CaM.

(D) Ca^{2+} regulation of Na channels can be triggered by Ca^{2+} influx through nearby $Ca_V2.1$ channels (Figures 3A–3D). Here, exemplar current records show that coexpression of mutant CaM_{1234} abolishes this modulation, confirming that CaM is the Ca^{2+} sensor for regulation of $Na_V1.4$ channels. Format as in Figures 3B–3D. Each symbol represents mean ± SEM.

(E) Population data plots Ca^{2+} regulation metric r_{Na} (Figure 3G) as a function of interpulse voltage V_{inter}. Format as in main text Figure 3G. Indeed, coexpression of CaM_{1234} abolishes CDI of $Na_V1.4$ channels, with rose fit reproduced from Figure 3G as reference. These results argue that Ca^{2+} regulation of $Na_V1.4$ observed with Ca^{2+} uncaging or Ca^{2+}-spillover from nearby $Ca_V2.1$ channels, both depend on the same process as mediated by CaM.

(F and G) Ca^{2+}/calmodulin-dependent protein kinase II (CaMKII) has been argued to phosphorylate $Na_V1.5$ channels (Aiba et al., 2010; Ashpole et al., 2012; Wagner and Maier, 2006). Though we found an absence of rapid Ca^{2+} regulatory effects on $Na_V1.5$ channels, could CaMKII play a role in the CDI of homologous $Na_V1.4$ channels? Here, extended data show that Na channel Ca^{2+}/CaM regulation does not require activation of Ca^{2+}/calmodulin-dependent protein kinase II (CaMKII) by application of KN-93, a blocker of CaMKII activity.

(F) Left, exemplar $Na_V1.4$ currents exhibit robust CDI. Right, this robust CDI is preserved following the application of 0.5 μM KN-93 for 3-30 min. Indeed, the kinetics and steady-state extent of CDI appear unaltered by inhibition of CaMKII. Format as in Figure 2A.

(G) Population data (black symbols) confirm that application of KN-93 does not alter the steady-state CDI versus Ca^{2+} relationship. Gray fit, control CDI versus Ca^{2+} relationship for $Na_V1.4$ channels (from main text Figure 2B). Overall, these results demonstrate that CDI of Na channels does not require CaMKII activation, further strengthening the case for CaM as a direct modulator of Na channels.

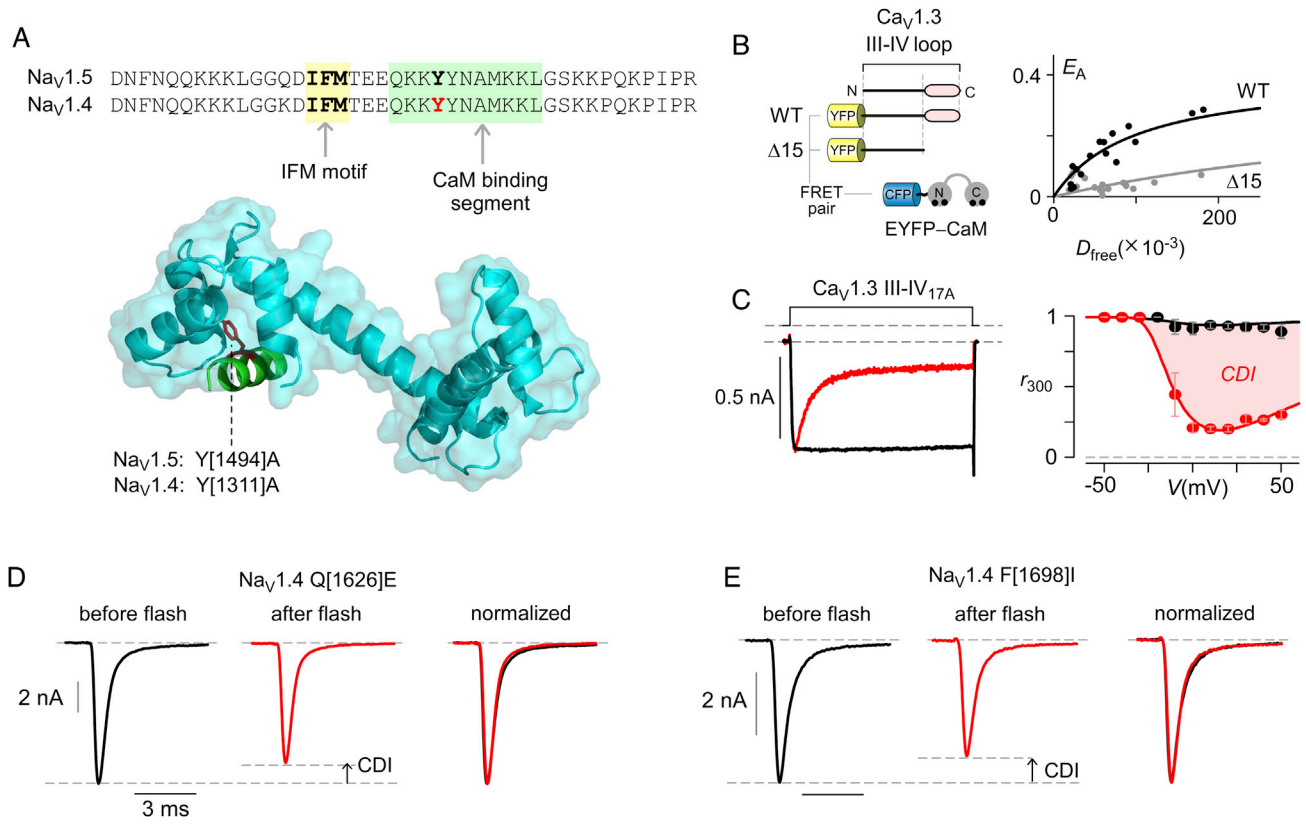

Figure S7. Ca^{2+}/CaM Binding to III-IV Loop of Both Ca^{2+} and Na Channels Nonessential for CDI and Kinetics of Channelopathic Mutant $Na_V1.4$ Channels, Related to Figures 5 and 6

(A) Top, sequence alignment of $Na_V1.4$ and $Na_V1.5$ III-IV loop. The proximity of this binding site to a primary structural determinant of fast inactivation localized to the tri-residue "IFM" motif (West et al., 1992) (yellow shading) is also diagrammed. Ca^{2+}/CaM binding site within the Na channel III-IV loop is highlighted in green. The critical Y[1311] residue mutated in main text Figure S6A is shown in red. Bottom, the crystal structure of $Na_V1.5$ III-IV loop bound to Ca^{2+}/CaM (PDB code: 4DJC [Sarhan et al., 2012]). Engagement of the critical tyrosine residue ($Na_V1.5$, Y[1494]; $Na_V1.4$, Y[1311]) is colored in red. This configuration has been argued to be a trigger for Ca^{2+} regulation of $Na_V1.5$, an outcome not observed in the present study. By contrast, we find that the carboxy tail of Na_V channels constitutes a prime structural determinant of CDI, not the III-IV loop.

(B) Similar to Na channels, the Ca^{2+} channel ($Ca_V1.3$) III-IV loop also contains a Ca^{2+}/CaM binding site. To evaluate this binding site, we conducted FRET 2-hybrid experiments of Ca^{2+}/CaM binding to both the full-length III-IV loop segment and a variant with a 15-residue deletion from the carboxy-terminal end of this segment (Δ15). Left, cartoon depicts FRET pairs used in this experiment. Right, plotting FRET efficiency (E_A) as a function of D_{free} (relative free concentration of ECFP-CaM) reveals a binding relation for full-length III-IV loop (black symbols and fit). The Δ15 mutant of the III-IV loop diminishes Ca^{2+}/CaM binding significantly (gray symbols and fit). For these experiments, we cotransfected CFP-tagged CaM with YFP-tagged III-IV loop channel segments in HEK293 cells cultured on glass-bottom dishes, and measured fluorescence intensities using an inverted fluorescence microscope as extensively described by our laboratory (Ben Johny et al., 2013; Erickson et al., 2001, 2003). Intracellular Ca^{2+} was elevated by using an external solution containing 10 mM Ca^{2+} and bath application of 4 μM ionomycin (Sigma-Aldrich, MO). The 3^3-FRET efficiencies (E_A) were computed as elaborated in our prior publications (Erickson et al., 2001).

(C) The functional relevance of this novel Ca^{2+}/CaM binding site on $Ca_V1.3$ III-IV loop was probed by substitution of the last 17 residues with alanines, since the deletion of this segment was detrimental to channel expression. Indeed, this manipulation spared CDI of Ca^{2+} channels. Left, exemplar currents for this mutant channel. Right, population average of r_{300} CDI metric defined in Figure 1C. Each symbol corresponds to mean ± SEM. These results reveal yet another commonality between Na and Ca^{2+} channels: both channel types contain a Ca^{2+}/CaM binding site within the III-IV loop, but this binding site does not seem to support CDI in either context. Nonetheless, this site may prove important in other aspects of channel function, such as channel trafficking.

(D) Invariance of kinetics for $Na_V1.4$ Q1626E current upon Ca^{2+} elevation. Left, $Na_V1.4$ Q1626E current before Ca^{2+} uncaging (Pulse #1 main text Figure 6C). Middle, Na current amplitude after Ca^{2+} uncaging (pulse #11 obtained ~450 ms after Ca^{2+} uncaging) is reduced by ~15%. Right, normalized current after uncaging shows unperturbed activation and inactivation kinetics in presence of Ca^{2+} (red trace after uncaging plotted on top of black trace before uncaging).

(E) Invariance of kinetics for $Na_V1.4$ F1698I current upon Ca^{2+} elevation. Format as in panel D above.